AMERICAN SOCIETY FOR MICROBIOLOGY | Journal of Bacteriology®

RESEARCH ARTICLE

Magnesium Modulates *Bacillus subtilis* Cell Division Frequency

Tingfeng Guo,[a] **Jennifer K. Herman**[a]

[a]Department of Biochemistry and Biophysics, Texas A&M University, College Station, Texas, USA

ABSTRACT By chance, we discovered a window of extracellular magnesium (Mg^{2+}) availability that modulates the division frequency of *Bacillus subtilis* without affecting its growth rate. In this window, cells grown with excess Mg^{2+} produce shorter cells than do those grown in unsupplemented medium. The Mg^{2+}-responsive adjustment in cell length occurs in both rich and minimal media as well as in domesticated and undomesticated strains. Of other divalent cations tested, manganese (Mn^{2+}) and zinc (Zn^{2+}) also resulted in cell shortening, but this occurred only at concentrations that affected growth. Cell length decreased proportionally with increasing Mg^{2+} from 0.2 mM to 4.0 mM, with little or no detectable change being observed in labile, intracellular Mg^{2+}, based on a riboswitch reporter. Cells grown in excess Mg^{2+} had fewer nucleoids and possessed more FtsZ-rings per unit cell length, consistent with the increased division frequency. Remarkably, when shifting cells from unsupplemented to supplemented medium, more than half of the cell length decrease occurred in the first 10 min, consistent with rapid division onset. Relative to unsupplemented cells, cells growing at steady-state with excess Mg^{2+} showed an enhanced expression of a large number of SigB-regulated genes and the activation of the Fur, MntR, and Zur regulons. Thus, by manipulating the availability of one nutrient, we were able to uncouple the growth rate from the division frequency and identify transcriptional changes that suggest that cell division is accompanied by the general stress response and an enhanced demand to sequester and/or increase the uptake of iron, Mn^{2+}, and Zn^{2+}.

IMPORTANCE The signals that cells use to trigger cell division are unknown. Although division is often considered intrinsic to the cell cycle, microorganisms can continue to grow and repeat rounds of DNA replication without dividing, indicating that cycles of division can be skipped. Here, we show that by manipulating a single nutrient, namely, Mg^{2+}, cell division can be uncoupled from the growth rate. This finding can be applied to investigate the nature of the cell division signal(s).

KEYWORDS *Bacillus*, LB, magnesium, manganese, SigB, UppS, zinc, cell division, morphology, undecaprenyl

The abundant cation Mg^{2+} is perhaps most appreciated for its role as an enzymatic cofactor, as it supports catalysis in hundreds of biochemical reactions (1–3). However, Mg^{2+} has diverse biological functions and is also critical for the assembly of ribosomes (4, 5), chelation, the stabilization of ATP and other polyphosphates (6), the regulation of phosphate uptake (7, 8), osmotic adaptation (9), the setting of the circadian period in plants (10), and the support of envelope integrity in bacteria (11–13). Due to the central place of Mg^{2+} in physiology, cells must be able to respond rapidly when availability fluctuates, as these fluctuations sometimes occur over several orders of magnitude. In human serum, where Mg^{2+} concentration is tightly controlled, 0.7 to 1.0 mM is considered homeostatic (14). In contrast, Mg^{2+} in the digestive tract of animals or in soil and aquatic environments is much more variable, ranging from micromolar to millimolar levels.

Whereas free-living bacteria can adapt to large fluctuations in extracellular Mg^{2+}, they keep intracellular levels relatively constant. Under replete conditions, cell-

Editor Tina M. Henkin, Ohio State University

Address correspondence to Jennifer K. Herman, jkherman@tamu.edu.

The authors declare no conflict of interest.

Received 3 October 2022
Accepted 28 November 2022

associated Mg^{2+} in *E. coli* is estimated to be 20 to 100 mM (15, 16), of which only 1 to 10 mM is considered labile (16–19). Of the remaining pool, approximately half is associated with nucleic acid, proteins, and ribosomes. The other half is found complexed with the enzymatically relevant form of ATP, the relatively stable chelate Mg^{2+}-ATP (20). Not surprisingly, ATP synthesis is tightly coordinated with Mg^{2+} availability (6). In fact, cells will scavenge Mg^{2+} from ribosomes at the expense of protein synthesis before allowing intracellular Mg^{2+} to fall to levels that are insufficient to support ATP chelation (6, 9, 21).

Intracellular Mg^{2+} is acquired using importer proteins that, in Gram-negatives, are often regulated by PhoPQ two-component systems (22, 23). These systems sense and respond to changes in both external Mg^{2+} availability and cellular demand primarily by regulating the transcription of Mg^{2+} transporters. *B. subtilis* lacks a homologous two-component system and controls the expression of its major Mg^{2+} importer (MgtE) via a riboswitch. The M-box riboswitch attenuates the transcription of *mgtE* when intracellular Mg^{2+} is sufficient by forming a terminator (4). Two other importers, YfjQ and CitM, also contribute to Mg^{2+} uptake (24). YfjQ is a minor importer, whereas CitM is a symporter that allows for the cotransport of Mg^{2+} and citrate (25, 26). Under hyperosmotic conditions and concomitant with potassium influx, *B. subtilis* can also efflux Mg^{2+} through an exporter called MpfA (27).

Aside from its role in supporting basic physiological functions, Mg^{2+} is known to suppress phenotypes associated with the inactivation of cell envelope-related genes. The provision of 10 to 25 mM Mg^{2+} (more than an order of magnitude higher than the concentrations found in typical media) restores both viability and rod shape to strains with deletions in the morphogenes *mreB*, *mbl*, *mreBH*, *mreC*, and *mreD* (28–30). Mg^{2+} restores a regular rod shape to strains with deletions in *ponA* (encoding PBP1A) and *lytE* (a major D, L-endopeptidase) (11, 31) as well as to strains with mutations in teichoic acid synthesis genes (12, 32, 33). A Δ*glmR* mutant, which is unable to upregulate gluconeogenesis, is inviable when grown on a gluconeogenic carbon source (34). Remarkably, millimolar Mg^{2+} can suppress this lethality (34). Mg^{2+} even increases resistance to the cell wall-targeting antibiotic methicillin (35). Thus, Mg^{2+} elicits cellular changes that allow it to function as a general suppressor of a wide variety of envelope-related defects.

The mechanism by which Mg^{2+} promotes envelope integrity is unclear. *B. subtilis* grown with higher levels of Mg^{2+} display lower levels of amidated meso-diaminopimelic acid in their peptidoglycan (PG) (36); however, reduced amidation itself is unlikely to account for Mg^{2+} rescue, as a mutant lacking the modification (Δ*asnB*) also has shape defects that are suppressed by Mg^{2+} (36). Mg^{2+} also reduces the dysregulated D, L-endopeptidase activity that is associated with deletion of *mreB* (37); it is unknown whether the impact of Mg^{2+} on endopeptidase activity is direct or is a consequence of other effects that Mg^{2+} has on the cell.

Here, we investigate a phenotype not previously associated with Mg^{2+}. We identify a window in which increasing Mg^{2+} availability increases the frequency of cell division without affecting the growth rate. Our results suggest that as Mg^{2+} availability decreases, cells prioritize the maintenance of cell elongation and growth over cell division. This prioritization of cell resources, which transcriptional profiling suggests is accompanied by changes in metal homeostasis and in the general stress response, results in longer cells with more nucleoids and fewer Z-rings.

RESULTS

Mg^{2+} supplementation leads to cell shortening in rich media in both domestic and undomesticated *B. subtilis* strains. In 2017, we obtained a new bottle of premade LB-Lennox powder from Sigma. While examining micrographs of membrane-stained *B. subtilis* 168 cells that were grown in liquid LB made from the new powder (LB*), we noted that the cells appeared qualitatively longer, compared to cells grown in previous lots of LB. LB is a rich medium consisting of only NaCl, tryptone, and yeast extract. We reasoned that the longer cells most likely resulted from a difference in trace element content. Mg^{2+} was a priority candidate both because tryptone-based media, such as LB, tend to be low in Mg^{2+} (37, 38) and because prior studies had shown that

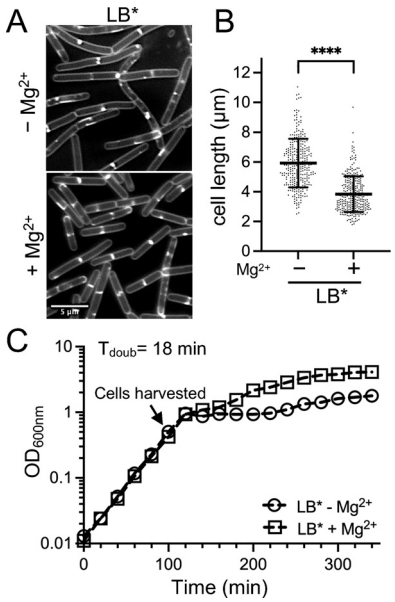

FIG 1 Cell length following growth in LB. WT *B. subtilis* 168 (BJH004) was grown at 37°C to the mid-exponential phase in LB* medium without or with 10.0 mM $MgCl_2$ supplementation. LB* indicates that the phenotype was lot-specific and is not generalizable to all LB. (A) Micrographs following the membrane staining and epifluorescence microscopy (scaled identically). (B) Scatterplots showing the distribution of cell lengths quantitated for 300 cells from each condition. The bars represent the means of 300 cells ± the SDs. (C) Representative growth curves. ****, $P \leq 0.0001$.

low Mg^{2+} media results in *B. subtilis* filamentation (39–41). We could not directly compare our results to those of published studies, as their microscopy methods did not include the visualization of septa present along filaments. To test whether the longer cells could be the result of low Mg^{2+} content in the new LB, we supplemented the medium with 10.0 mM $MgCl_2$ and imaged cells following membrane staining. As shown in Fig. 1A and B, cells grown with supplemental Mg^{2+} were 36% shorter on average, consistent with the possibility that the cells were longer in the new medium due to the reduced Mg^{2+} content.

Since the growth rate can affect the cell size (42–48), we next assessed whether the Mg^{2+} addition affected the doubling time of the cells in the new LB. We found that the growth rates of cells cultured without and with 10.0 mM $MgCl_2$ were identical during the exponential stage (Fig. 1C), the same phase of growth used for cell imaging. From these results, we concluded that there is a growth rate-independent effect of Mg^{2+} availability on cell length, at least in the window tested.

The phenotype that we initially observed was specific to only one batch of LB. So, we next investigated whether the Mg^{2+} responsive phenotype could be observed in another rich medium. CH (casein hydrolysate) is an amino acid-based medium (49) that is commonly used in *B. subtilis* studies. We found that *B. subtilis* grew robustly in CH without the standard addition of Mg^{2+} and Mn^{2+} salts (Fig. 2A) and designated this medium CH*. Similar to the results with LB*, the cells grown in CH* exhibited a Mg^{2+}-responsive phenotype. *B. subtilis* 168 cells cultured in CH* with 10.0 mM Mg^{2+} were approximately 2-fold reduced in average cell length, compared to those cultured in CH* only (Fig. 2B and C). No difference in doubling time (Fig. 2A) or cell width (Fig. 2D) was detected between CH* and CH* supplemented with Mg^{2+}.

Next, we investigated whether the Mg^{2+}-responsive phenotype observed in the *B. subtilis* 168 cells was present in two other commonly utilized *B. subtilis* strains: the SPβ-cured laboratory strain PY79 (50) and the undomesticated strain NCIB 3610 (50). Independent of strain, the addition of 10.0 mM $MgCl_2$ to CH* consistently resulted in cells that were approximately 2-fold reduced in length, compared to CH* alone (Fig. 2B

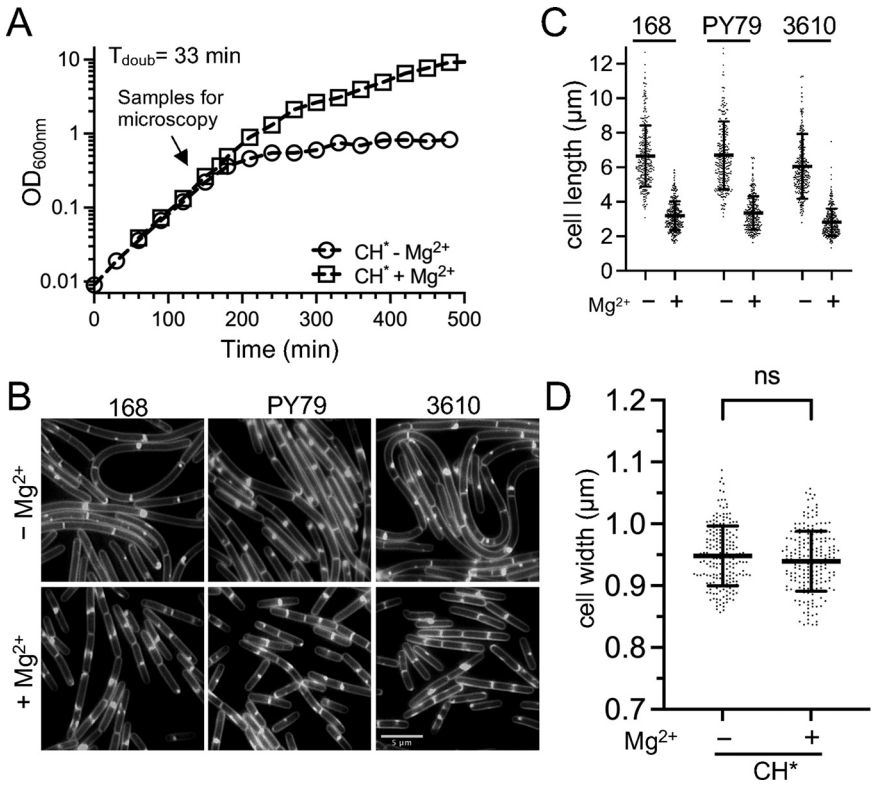

FIG 2 Cell length of three *B. subtilis* strains following growth in CH* medium. WT *B. subtilis* 168 (BJH004), PY79 (BJH001), and 3610 (BJH403) were grown at 37°C to the mid-exponential phase in CH* supplemented with 10.0 mM $MgCl_2$ as indicated. (A) Representative growth curves for the WT. (B) Representative micrographs following the membrane staining and epifluorescence microscopy (scaled identically). (C) Scatterplots showing the distribution of cell with quantitated for 300 cells from each condition. The bars represent the means of 300 cells ± the SDs. (D) Scatterplots showing the distribution of cell widths for 200 cells grown without or with 10.0 mM $MgCl_2$. The bars represent the means of 200 cells ± the SDs. ns, $P > 0.05$.

and C). These results suggest that the effect of Mg^{2+} is likely to be a phenomenon that is generalizable to the species.

Mn^{2+} and Zn^{2+} supplementation also elicit cell shortening. We wondered whether the growth rate-independent cell shortening was specific to Mg^{2+} or could also be induced by providing other metals in excess. For these experiments, we again utilized CH*. Cells were grown as before, but instead of supplementing cultures with $MgCl_2$, salts of Ca^{2+}, Cu^{2+}, Fe^{2+}, Fe^{3+}, Mn^{2+}, and Zn^{2+} were added. Of the metals tested, only Mn^{2+} and Zn^{2+} elicited cell shortening similar to that observed for Mg^{2+} (Fig. 3; Fig. S1); however, Zn^{2+} strongly reduced the growth rate at the concentrations required to observe the cell shortening effect (0.2 mM) (Fig. S1). While Mn^{2+} did not reduce the doubling time of cells once the culture reached the exponential phase, the precultures containing Mn^{2+} remained in lag for several hours longer than did the unsupplemented cultures. Due to the pleiotropic effects of Zn^{2+} and Mn^{2+} on the growth, we chose to focus on Mg^{2+} for the remainder of the study.

The Mg^{2+}-responsive phenotype occurs in minimal medium and does not require the addition of exogenous amino acids. Minimal media (MM) allows for the manipulation of individual medium components but generally results in a slower doubling time because it requires that cells undertake extensive *de novo* synthesis. To test whether Mg^{2+} could modulate cell length in a defined medium, we utilized a phosphate-buffered glucose MM. We began with a base medium that contained 13 amino acids and 50.0 μM Mg^{2+} (MM-13aa). In MM-13aa, the doubling time for the *B. subtilis* 168 prototroph (functional *trpC*+) was 53 min, both with and without the addition of 10.0 mM $MgCl_2$ (Fig. 4A). The cell length in MM-13aa was assessed using microscopy

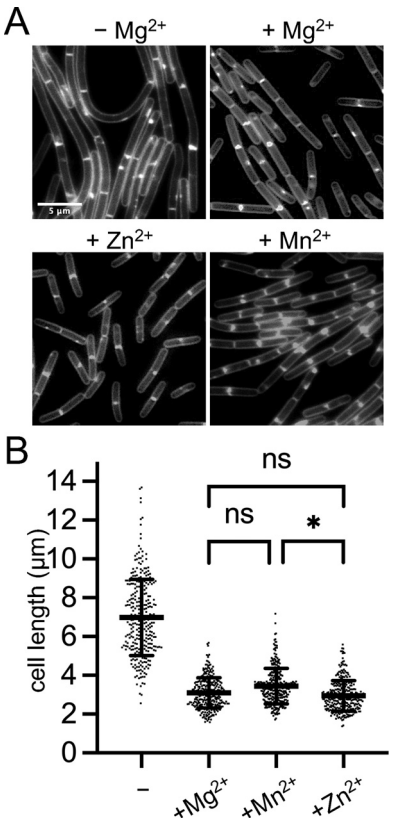

FIG 3 Effect of divalent metals on cell length. WT 168 (BJH004) cells were cultured in CH* without or with the following concentrations of divalent cation salts: 0.1 mM $MnSO_4$, 0.2 mM $ZnCl_2$, 10.0 mM $MgCl_2$. (A) Micrographs following the membrane staining and epifluorescence microscopy (scaled identically). (B) Scatterplots showing the distribution of cell lengths quantitated for 300 cells from each condition. The bars represent the means of 300 cells ± the SDs. *, $0.01 < P \leq 0.05$; ns, $P \geq 0.05$. For all pairwise comparisons to the control without additional metal (−), a P value of <0.0001 was calculated.

and quantitation. As shown in Fig. 4B and C, the cells grown with supplemental Mg^{2+} were 45% shorter than those grown in MM-13aa only.

To test whether the Mg^{2+}-responsive phenotype was dependent on the presence of amino acids in the medium, the experiments were repeated in the base MM without amino acid supplementation. This modification increased the doubling time to 59 min, but the growth rate again remained unchanged, both with and without Mg^{2+} supplementation (Fig. 4A). Similar to the pattern observed in the media that contained amino acids (LB, CH*, and MM-13aa), the cells were shorter in the Mg^{2+} supplemented medium, compared to those in the unsupplemented control (Fig. 4B and C). These results suggest that the Mg^{2+}-responsive phenotype is generalizable to both complex and defined media and does not depend on the addition of amino acids.

Mg^{2+}-responsive cell length changes follow a dose-response curve. Next, we wanted to know whether cell length decreased proportionally with increasing extracellular Mg^{2+} or, alternatively, there was a threshold at which cells underwent a switch in cell length. To investigate this, we cultured cells in media across a range of Mg^{2+} concentrations, from 6.25 μM $MgCl_2$ (at which differences in the growth rate begin to emerge at the densities at which we collected the cells) (Fig. 5A) up to 25.0 mM. Cells from each condition were imaged, and the cell lengths were quantified (Fig. 5). We found that cell shortening was neither directly proportional to Mg^{2+} availability nor a switch. Instead, cells became progressively shorter from 12.5 μM to 4.0 mM, with the largest decrease occurring between 0.2 μM and 2.0 mM (Fig. 5C and D).

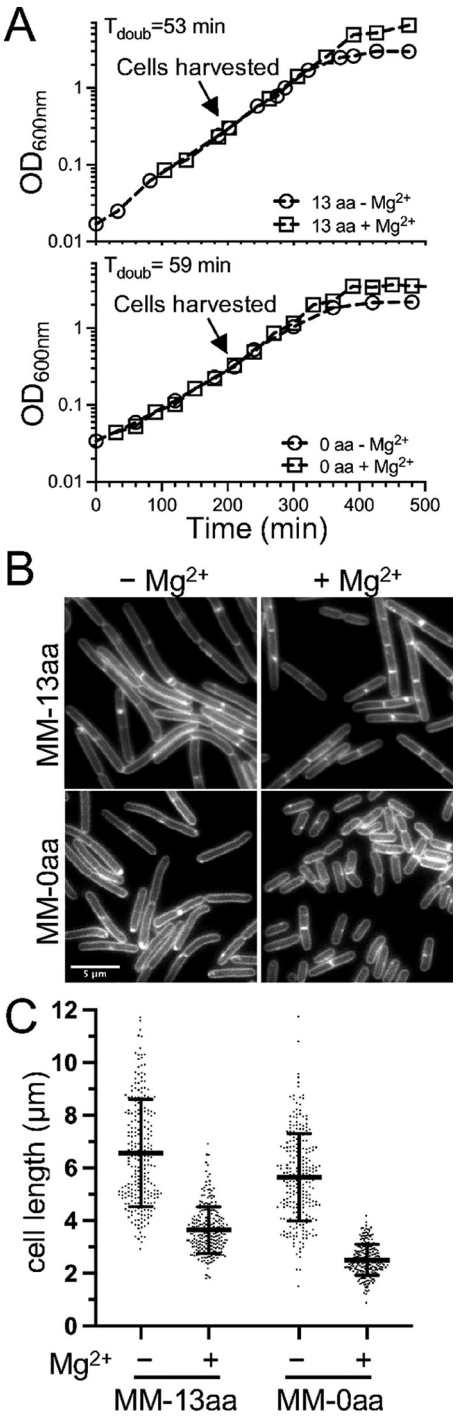

FIG 4 Cell length of *B. subtilis* following growth in minimal medium (MM). WT *B. subtilis* 168 (*trpC* prototroph) (BTG169) was cultured in a base MM containing 50.0 μM Mg^{2+} supplemented with 10.0 mM $MgCl_2$ and amino acids as indicated. (A) Representative growth curves. (B) Micrographs following the membrane staining and epifluorescence microscopy (scaled identically). (C) Scatterplots showing the distribution of cell lengths quantitated for 250 cells from each condition. The bars represent the means of 250 cells $\pm$ the SDs.

Cells in the 0.2 μM to 2.0 mM window grew at equivalent doubling times (Fig. 5A), suggesting that the cells were not yet experiencing significant intracellular Mg^{2+} limitation. To independently assess this, we introduced a promoter fusion (P_{mgtE}-*lacZ*) that reports on changes in internal Mg^{2+} availability. The promoter region includes a riboswitch that terminates transcription when the intracellular Mg^{2+} levels are sufficient

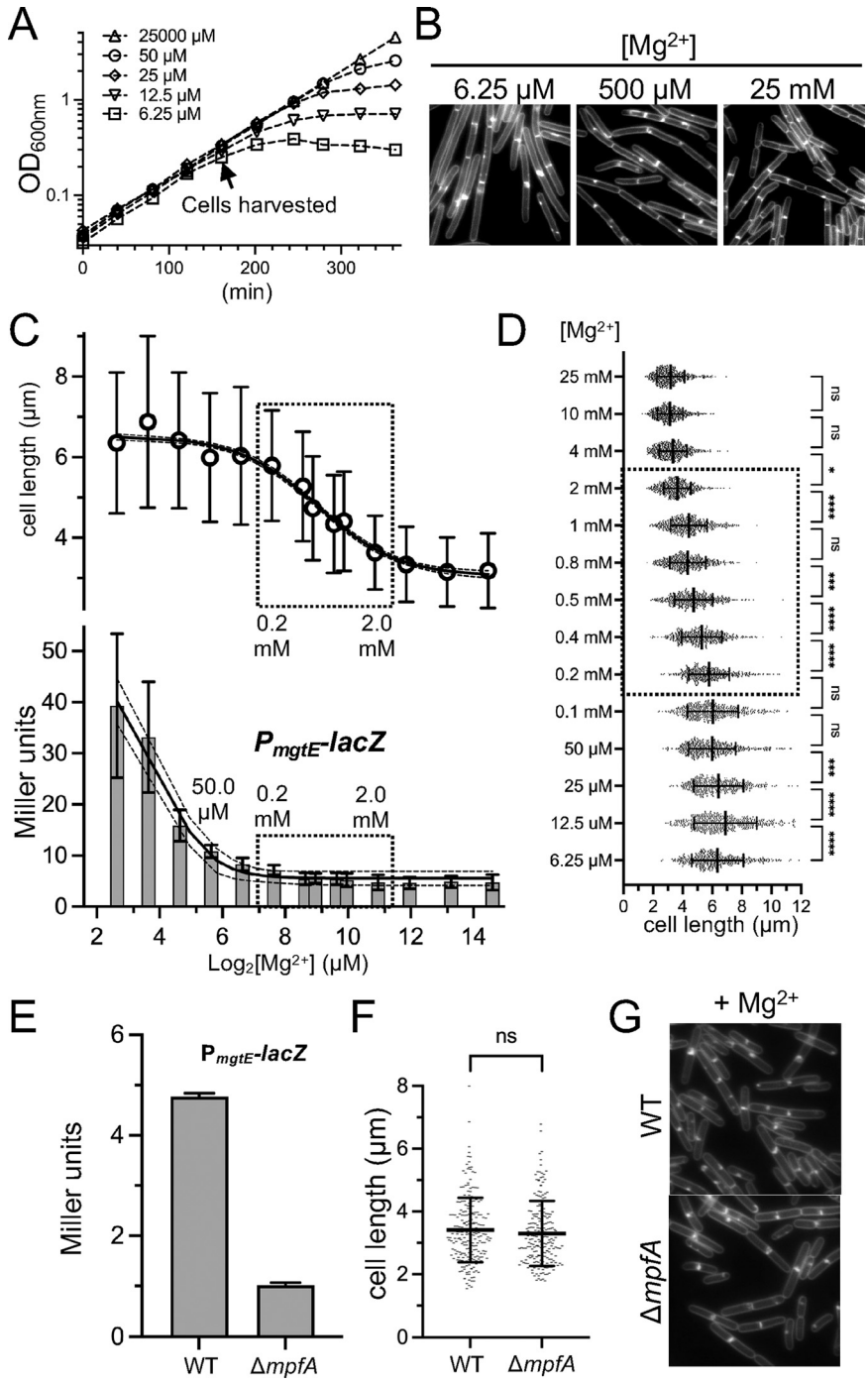

FIG 5 Correlation analysis of extracellular Mg^{2+} availability with cell length and with a reporter of intracellular Mg^{2+}. WT cells harboring a reporter for P_{mgtE}-*lacZ* (BTG182) were grown in MM-13aa with the indicated concentrations of supplemental $MgCl_2$. (A) Representative growth curves and (B) representative micrographs following the membrane staining (scaled identically) from across the range of Mg^{2+} concentrations examined. (C) Mean cell lengths for 500 cells ± the SD for each condition (top) and the β-galactosidase activity assay for the *mgtE* riboswitch transcriptional reporter (bottom). (D) Scatterplots showing the distribution of cell lengths at each Mg^{2+} concentration. The bars represent the mean cell lengths for 500 cells ± the SDs. (E–G) WT (BTG182) or the Δ*mpfA* mutant (BTG333) harboring a reporter for P_{mgtE}-*lacZ* was grown in MM-13aa supplemented with 10.0 mM $MgCl_2$. Samples were taken during the exponential growth phase. (E) β-galactosidase activity assay. The bars represent the means from 2 biological replicates ± the SDs. (F) Scatterplots showing the distribution of cell lengths. The bars represent the mean cell lengths for 200 cells ± the SDs. (G) Representative micrographs of cells stained with TMA and scaled identically. *, $0.01 < P \leq 0.05$; **, $0.001 < P \leq 0.01$; ***, $0.0001 < P \leq 0.001$; ****, $P < 0.0001$; (ns) $P \geq 0.05$.

(51, 52). Using this reporter, Dann et al. observed an approximately 10-fold induction of LacZ activity following the extended growth of cells with 5.0 μM Mg^{2+} (growth rate-limiting), compared to a Mg^{2+} excess (2.5 mM in their study) (Fig. 1B in reference [51]). Consistent with these findings, we observed that LacZ activity was also induced in medium containing 6.25 μM Mg^{2+} (Fig. 5B). Notably, this induction coincided with the time when the growth rate effects began to be observable (Fig. 5A).

The steepest decline in cell-shortening occurred between 0.2 and 2.0 mM $MgCl_2$. To our surprise, no substantial differences in P_{mgtE}-*lacZ* activity were detectable in this window, suggesting that the cell shortening is unlikely to be attributable to increased levels of labile intracellular Mg^{2+}. We considered the possibility that the riboswitch of the P_{mgtE}-*lacZ* reporter may already be saturated (terminator form) in this range and thus may be insensitive to further increases. To test this, we deleted the gene for the Mg^{2+} exporter protein MpfA, which was previously shown to increase intracellular Mg^{2+} (53). Even when cells were grown in 10.0 mM $MgCl_2$, the Δ*mpfA* mutant displayed an additional 4-fold reduction in LacZ activity, compared to the wild-type (Fig. 5E), indicating that the reporter retained sensitivity. This result suggests that if there are changes in intracellular Mg^{2+} in the range in which we observe the most dramatic decreases in cell length, then the changes are not detectable with our reporter. Notably, even though intracellular Mg^{2+} can be inferred to have increased in the Δ*mpfA* mutant, compared to the wild-type, no differences in average cell length were observed (Fig. 5F and G). Collectively, these results suggest that under our growth conditions, changes in intracellular labile Mg^{2+} are neither necessary nor sufficient to elicit cell shortening. At the same time, we do not exclude the possibility that the cells may be responding to changes in intracellular Mg^{2+} that are not detectable by P_{mgtE}-*lacZ*, such as an increase in the nonlabile pool. An alternative possibility is that the response is driven by differences in extracellular, or at least extracytoplasmic, Mg^{2+}.

Cell shortening following a shift from lower to higher Mg^{2+} is rapid. In the experiments above, the cell lengths were determined during steady-state growth, and care was taken to collect the cells at equivalent densities, as Mg^{2+} continues to be depleted from the medium with time. To assess the transition from longer to shorter, we grew cells in CH* and in MM-13aa, and we monitored the lengths of the cells at 10 min intervals after the addition of 10.0 mM $MgCl_2$ (Fig. 6). For both media, the mean cell length continued to decrease for 40 to 50 min, at which point the cells achieved a mean length similar to those of cells always grown with excess Mg^{2+} (Fig. 6). Remarkably, 54% and 40% of the total decrease in the mean cell length occurred within the first 10 min of adding Mg^{2+} in the CH* and MM-13aa media, respectively (Fig. 6). Thus, the initial response to Mg^{2+} is relatively rapid and is well below the doubling time of the cells. After the initial rapid decrease, a more gradual decline in average cell length was observed. These results suggest that the adjustment to higher Mg^{2+} may occur through two distinct mechanisms: a dramatic initial decrease in cell length resulting from rapid division onset and a second, more protracted period in which the average cell length decreases more incrementally. These observations suggest that the initial response may have a more biophysical or enzymatic basis, whereas the second requires biosynthesis and outgrowth to achieve a new steady-state length.

Mg^{2+} modulates the frequency of Z-ring assembly. A rod-shaped bacterium can increase cell length without altering other dimensions by elongating faster, dividing less frequently, or both. Based on the optical density, the growth rate of the cells in our experiments was equivalent, both with and without Mg^{2+} supplementation. Although absorbance readings are the most widely accepted method for monitoring cell growth, we considered the possibility that the populations that we were comparing might absorb light differently enough to mask differences in mass accumulation. To independently test this, we examined the abundance of the constitutively expressed protein SigA via a western blot analysis. In both CH* and MM-13aa, the SigA levels were equivalent, with and without Mg^{2+} supplementation, when cells were normalized to each other using OD_{600} values (Fig. S2A). As an additional control, we compared the dry weights of samples grown in MM-13aa with and without excess Mg^{2+} (Fig. S2B). The dry weights were indistinguishable in the two conditions, further supporting the conclusion that the optical density provides an accurate approximation of the cell mass. These results strongly support the conclusion that

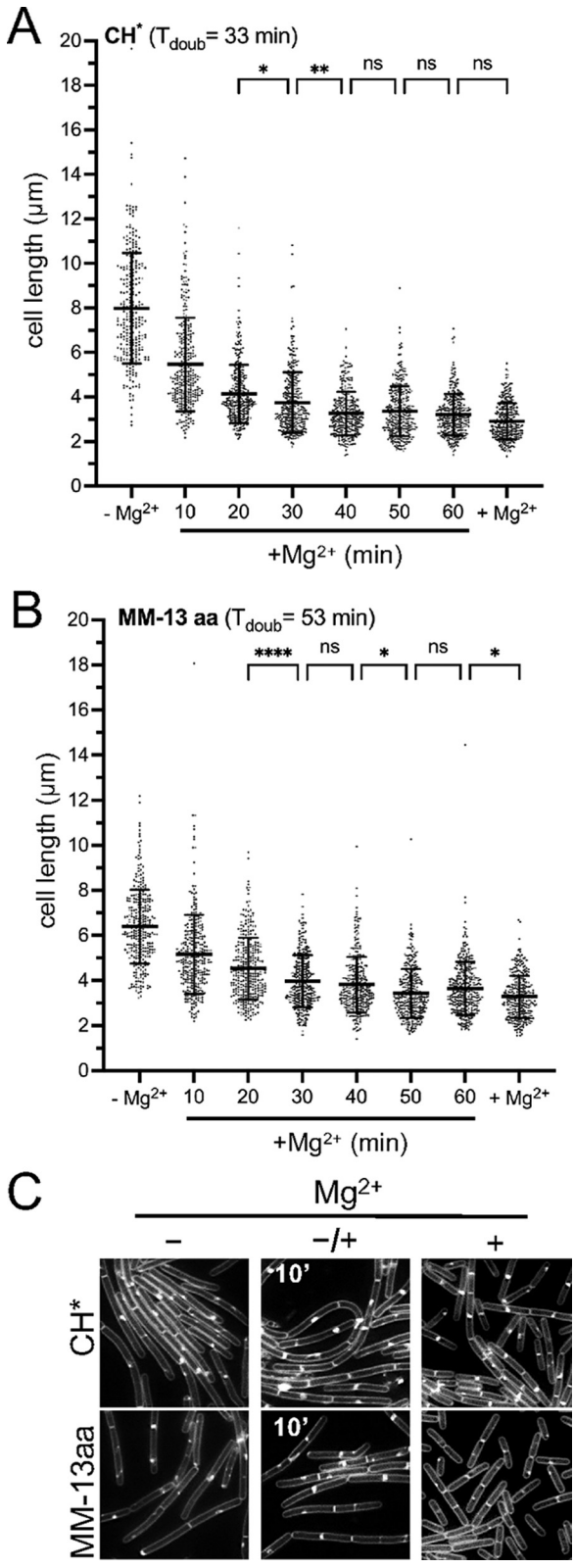

FIG 6 The *B. subtilis* cell length response to a change in extracellular Mg^{2+} is fast and is independent of the growth rate. WT 168 (BJH004) was cultured in the indicated media without Mg^{2+} supplementation (–Mg^{2+}). Following addition of 10.0 mM $MgCl_2$, the cells were imaged at 10 min intervals. (A and B) The bars represent the mean cell lengths for 300 cells ± the SDs. (C) Representative micrographs. The membranes are stained with TMA, and the images are scaled identically. *, $0.01 < P \leq 0.05$; **, $0.001 < P \leq 0.01$; ****, $P < 0.0001$; (ns) $P \geq 0.05$.

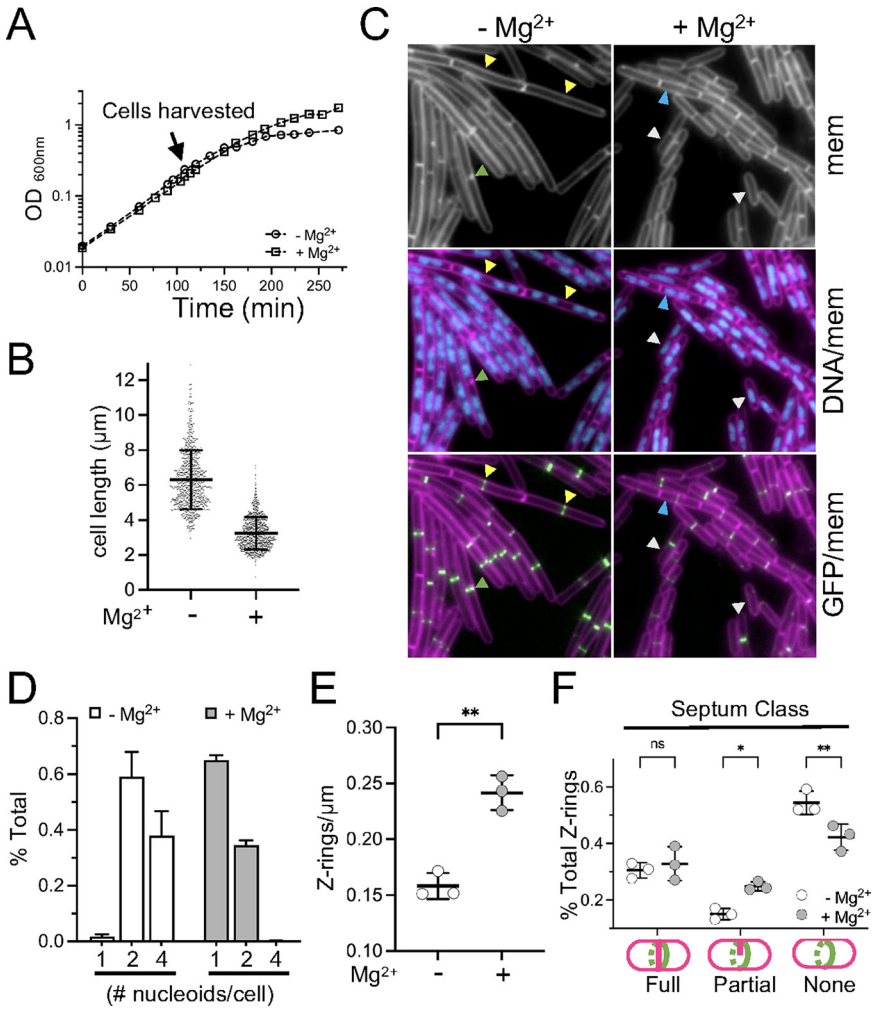

FIG 7 Mg^{2+} modulates the frequency of Z-ring assembly. WT cells harboring P_{xyl}-*GFP-zapA* (BTG186) were cultured in CH* with 2.0 mM xylose. 10.0 mM $MgCl_2$ was added as indicated. (A) Representative growth curves. (B) Scatterplots showing the distribution of cell lengths. The bars represent the mean cell lengths of 800 cells ± the SDs. (C) Representative micrographs following the staining of membranes and nucleoids with FM4-64 and DAPI, respectively. The images are scaled identically. The arrowheads indicate examples of cells with four nucleoid masses and Z-rings that lack septa (yellow), 1 nucleoid mass (white), 2 nucleoid masses (blue), or partial septa (green). (D) Fraction of cells with the indicated number of nucleoids from three independent biological replicates. (E) Average number of Z-rings per unit cell length ± SD. Each circle represents the mean of 300 cells from three independent biological replicates per condition. (F) Average fraction of cells with coalesced ZapA-GFP that presented the indicated septum type ± the SD. Each circle represents the mean of 300 cells from three independent biological replicates per condition. *, $0.01 < P \leq 0.05$, **, $0.001 < P \leq 0.01$; (ns) $P \geq 0.05$.

Mg^{2+} supplemented cells become shorter as a result of more frequent cell divisions, and, conversely, that cells divide less often under lower Mg^{2+} conditions.

A delay in septation could occur before or after the assembly of the divisome. To assess this, we grew wild-type harboring a GFP fusion to ZapA, an early-arriving cell division protein that colocalizes with FtsZ as part of the "Z-ring" (54, 55). Cells expressing P_{xylA}-*GFP-zapA* grew equivalently, with and without 10.0 mM $MgCl_2$ (Fig. 7A), and retained the Mg^{2+}-responsive reduction in cell length (Fig. 7B and C). Epifluorescence microscopy was performed, and images were captured of membranes, DNA (nucleoids), and Z-rings from both conditions (Fig. 7B). Overlays of the micrographs were used to quantitate both the number of distinct nucleoids per cell (Fig. 7D) and the number of Z-rings per unit cell length (Fig. 7E).

Regardless of the condition, both populations possessed a large proportion of cells

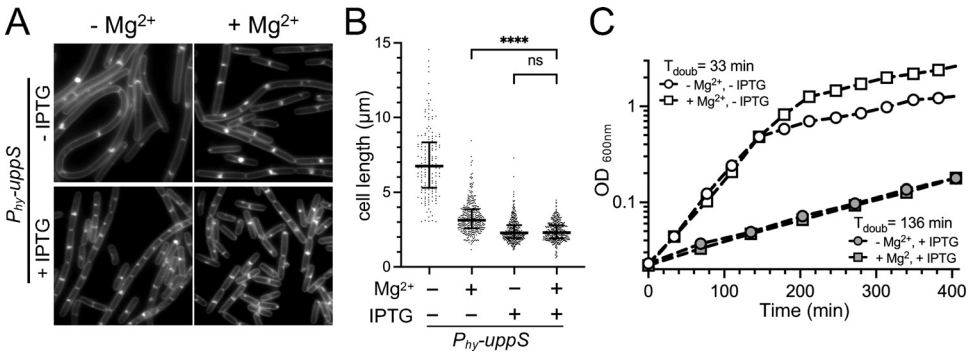

FIG 8 UppS overexpression results in constitutively short cells. WT cells harboring P_{hy}-*uppS* (BTG708) were cultured in CH* with $MgCl_2$ (10.0 mM) and IPTG (0.5 mM) added as indicated. (A) Representative micrographs of cells stained with TMA and scaled identically. (B) Scatterplots showing the distribution of cell lengths quantitated for 300 cells from each condition. The bars represent the mean cell length ± the SD. (C) Representative growth curves. ****, $P < 0.0001$; (ns) $P > 0.05$.

with two nucleoids (35% and 59% for the samples with and without supplemental Mg^{2+}, respectively). The most striking differences became apparent when comparing the proportions of cells with one or four nucleoids. While only 2% of the cells grown in CH* had one distinct nucleoid mass, this proportion increased 30-fold (to 65%) in the Mg^{2+}-supplemented medium. Conversely, cells with four nucleoids were relatively frequent (38%) in the base medium but were rare (<1%) in the Mg^{2+}-supplemented cultures (Fig. 7D). These results indicate that division is more frequent when Mg^{2+} is in excess. Consistent with this idea, Z-rings were more frequently observed along the lengths of Mg^{2+}-supplemented cells, and fewer Z-rings were observed along the lengths of cells grown in unsupplemented CH* (Fig. 7E). Moreover, the Z-rings that did form were less likely to be associated with a partial (incomplete) septum (Fig. 7F). Similar results were observed when FtsZ was tracked directly with an FtsZ-GFP fusion (Fig. S3). We conclude that there is a window of Mg^{2+} availability in which the cell division frequency can be modulated before the growth rate is impacted.

Overexpressing undecaprenyl pyrophosphate synthetase (UppS) results in the loss of the Mg^{2+}-responsive phenotype and in constitutively short cells. In the CH* shifting experiment, more than half of the decrease in the average cell length occurred within 10 min of adding the Mg^{2+} (Tdoub = 33 min) (Fig. 6), suggesting that a majority of the cells were generally poised to divide but were somehow inhibited. In a 1969 study, Garrett showed that Mg^{2+}, in the same ranges of interest as were examined in our study see Table 2 in reference [56]), caused *B. subtilis* (W23) to accumulate the cytoplasmic PG precursor UDP-MurNAc-pentapeptide (56). This result suggests that the next step in the PG synthesis pathway, namely, the generation of Lipid I via the conjugation of the MurNAc-pentapeptide to Und-P (Fig. S4A), is sensitive to Mg^{2+} availability.

Und-P is generated through the dephosphorylation of Und-PP, the latter of which is either synthesized *de novo* by UppS or is regenerated following the transfer of Und-P-linked precursors to acceptor molecules (Fig. S4A). To test whether increasing the Und-PP pools from the *de novo* synthesis pathway would promote more frequent division, we overexpressed *uppS* from an IPTG-inducible promoter. *uppS* overexpression resulted in shorter cells, compared to the uninduced control in CH*, and the overexpressing cells were equivalently short, irrespective of Mg^{2+} supplementation (Fig. 8A and B). In contrast, overexpressing *mraY*, which encodes the enzyme that reversibly transfers phospho-MurNAc-pentapeptide to Und-P (Fig. S4A) (57), did not shorten the cells, and the cells remained responsive to Mg^{2+} (Fig. S4B and 4C). In contrast, cells overexpressing *bcrC*, which encodes the major Und-PP phosphatase (58–60) (Fig. S4A), were 37% shorter in CH*, compared to the uninduced control (Fig. S4C and D), consistent with enhanced division. However, unlike *uppS*, *bcrC*-overexpressing cells were still able to decrease in length following the addition of Mg^{2+} (Fig. S4D). The growth rate of the cells overexpressing *uppS* was slower, but it was

equivalent with and without Mg^{2+} supplementation (Fig. 8C), suggesting that the cell length decrease is not simply attributable to the lower growth rate. At the same time, we cannot exclude the possibility that slow growth reduces the cells to a length that makes differences too subtle to be measured with our assay. Together, these results suggest that the availability of Und-P is rate-limiting for cell division in the unsupplemented medium.

RNA-seq analysis of cells grown with and without excess Mg^{2+}. To further explore the Mg^{2+}-responsive phenotype, we used an RNA-seq analysis to determine whether there were relative changes in transcription between the short and long cells that could provide insight into the mechanism. RNA-seq was performed using samples collected from exponential-phase cells that were growing in CH* or in CH* supplemented with 10.0 mM $MgCl_2$. Genes expressed either more or less in the Mg^{2+}-supplemented CH*, relative to CH* alone, were categorized based on known regulatory information that was retrieved from SubtiWiki (Tables S1 and S2) (61, 62).

As expected, based on the riboswitch data (Fig. 5), the transcriptional changes related to Mg^{2+} homeostasis were not significant. To our surprise, a number of other regulons that are related to metal homeostasis showed significant and internally consistent relative shifts in transcription. In particular, the profiles indicated the upregulation of the genes repressed by Fur (Fe^{2+} acquisition, sequestration, and sparing), MntR (Mn^{2+} uptake), and Zur (Zn^{2+} acquisition). In addition, there was enhanced expression of a large number of genes, consistent with a response to enhanced general stress (SigB). A subset of genes from two different prophages (PBSX and SPβ) were also expressed at higher levels but not in a manner consistent with prophage induction (Table S1). Conversely, and consistent with the observed upregulated genes, we observed the downregulation of the CzrA repressed genes *cadA*, *czcD*, and *trkA* (Zn^{2+} efflux/resistance to toxic metals), *mneP* (MntR-activated Mn^{2+} efflux), a large number of genes under the control of various cell envelope stress sigma factors (SigM/X/W/V), and those activated by the two-component response regulator YvrHb (63). Notably, several regulatory genes showed decreased transcription, including *rsiX* (encoding a SigX anti-sigma factor), *sigX*, and *abh* (a regulator of the transition state). Although we screened strains deleted for genes that showed differential expression via RNA-seq, those that were part of an annotated two-component system, and a strain that was cured of all prophages, each of the mutants retained the Mg^{2+}-responsive phenotype (Tables S1–S3). Thus, although metal homeostasis and general stress response genes are clearly impacted by the changes in Mg^{2+} availability, we currently lack data that link any of these changes to enhanced division.

DISCUSSION

The findings in this study surprised us in several ways. First, the discovery of the cell division phenotype was itself unanticipated. Although LB is known to be low in Mg^{2+} and is generally discouraged by cell physiologists for various reasons (nicely outlined in a Small Things Considered blogpost by Hiroshi Nikaido [64]), LB has also been the default medium for the routine propagation of *B. subtilis* and *E. coli* for decades - not necessarily a context in which one expects to observe a novel phenotype. We cannot definitively say whether or not the phenotype observed in LB (Fig. 1) was due to the unusually low level of Mg^{2+} in the batch, as the powder was exhausted, and its bottle and lot number were discarded long before we appreciated the significance of the phenotype. Nonetheless, the data strongly implicated Mg^{2+} and motivated further experiments, which ultimately demonstrated that reduced Mg^{2+} availability impacts division before the growth rate and cell elongation.

The finding itself makes sense intuitively, as cell division is not a prerequisite for the replication of genetic material, growth, or survival. In fact, many bacteria are known to subsist as filamentous forms that divide infrequently. An extreme version of the filamentous lifestyle was recently discovered in the marine organism *Thiomargarita magnifica*, which displays average lengths of nearly a centimeter (65). This remarkable bacterium was found to harbor approximately 37,000 copies of its genome per millimeter of cell length - evidence of a dramatic uncoupling between growth and cell division. It is notable that many of the longest bacteria ever recorded, including the giant

bacterium *Beggiatoa* that was discovered by Winogradsky, are sulfur-oxidizers (66). The evidence for an intimate relationship between sulfur metabolism and cell division is not restricted to giant bacteria. *E. coli* mutants with a reduced ability to convert ATP and the sulfur-containing amino acid methionine into S-adenosyl methionine (SAM) are inhibited for cell division but continue to grow and replicate DNA (67). The capacity of cells to uncouple division from other biosynthetic processes makes sense from an evolutionary perspective; it could provide cells with a mechanism by which to continue generating new "units" as resources deplete, while at the same time reserving the option to rapidly separate into individual cells when conditions are favorable.

Additional surprising results were the degree and type of the transcriptional changes that occurred between the supplemented and unsupplemented growth conditions. We expected that if changes occurred at all, then they would be associated with envelope synthesis or Mg^{2+} uptake or efflux. Instead, we observed changes in genes related to the general stress response and to iron, Mn^{2+}, and Zn^{2+} homeostasis. More specifically, we found that when Mg^{2+} is more available, the expression of the SigB regulon is enhanced, and the Fur, MntR, and Zur regulons undergo shifts consistent with acquisition, sequestration, and/or sparing responses.

At first, the metal responses were perplexing, as we are accustomed to thinking about most metal regulons in terms of responses to starvation or toxicity, conditions that were not present in our experiments. However, the responses are relative, not absolute, and we can think of several other ways to interpret the data. The first is to think of the changes as homeostatic adjustments. For example, the data indicate that in the higher Mg^{2+} condition, the cells receive signals consistent with the need to acquire, sequester, and spare iron, as well as to increase internal Mn^{2+} and Zn^{2+}. The expression of genes for surfactin biosynthesis (*srfABCD*) and the SigB general stress response are also increased. Iron sequestration and iron-sparing responses would reduce the possibility of Fenton reactions (68). Mn^{2+} and Zn^{2+} both reduce internal reactive oxygen species (69–75), and surfactin and SigB both combat oxidative/energy stress, the former by reducing proton motive force (76, 77). The overall profile suggests that, compared to the unsupplemented cells, the Mg^{2+}-supplemented cells exhibit changes consistent with the prevention of oxidative stress.

The second possibility, which is not mutually exclusive, is that at least some of the transcriptional changes are associated with events before, after, and/or during cell division itself. Cell cycle variations are typically obscured when samples are collected from pooled populations of asynchronously growing cells. The samples collected for RNA-seq were also growing asynchronously; however, because the Mg^{2+}-supplemented populations were essentially "enriched" for dividing cells (Fig. 7; Fig. S3), the transcriptional changes associated with division should also be enriched. The idea that cells may adjust metal pools not only to respond to different environmental stressors but also as a regulated part of the life cycle or development is intriguing, and we think it merits further inquiry.

We noted one anomaly in the RNA-seq data that we do not understand. In the Zur regulon, we see more RNA corresponding to *yczL* but relatively little or no increase in other genes found in the predicted (78) *folEB-yciB-yczL-zagA* transcript (Table S1). The unexpected differential expression of the *yczL* region could be attributable to differences in RNA stability, rather than transcription itself. The gene upstream of *yczL* (*yciB*) is proceeded by four instances of putative cotranslational coupling, the last of which could lead to the translation of *yczL*. It may be worth exploring whether there is a functional consequence to the predicted coupling, such as the alteration of transcriptional readthrough, transcript stability, or the effects on the expression of the downstream gene *zagA*.

We do not know whether any of the transcriptional changes relate directly to the Mg^{2+}-responsive phenotype or are incidental. We are uncertain whether differential expression would still occur if cells were grown at maximal "shortness" but different Mg^{2+} concentrations, such as the 4.0 mM to 25.0 mM range shown in Fig. 5. The cell shortening phenotype was still detected in a prophage-cured strain (Table S3). So, at

the least, the prophage-related changes appear to be incidental. Consistent with this conclusion, others have documented differential expression from various *B. subtilis* prophage loci as having resulted from variation the in growth regime (79).

Visually screening a number of deletion strains also failed to implicate any single gene knockouts in the Mg^{2+}-responsive phenotype (Tables S1–S3). The only condition identified that showed an apparent loss of Mg^{2+}-responsiveness in CH* was the overexpression of *uppS* (Fig. 8). However, as these cells grew slowly, we could not confidently exclude the possibilities that (i) cell shortening occurred but fell outside the detection limit of our assay and/or (ii) that the low growth rate imposes an upper limit on the division frequency that is dominant over the effects of Mg^{2+}.

Still, it is plausible that exogenous Mg^{2+} somehow enhances the availability of Und-P to the divisome. UppS utilizes Mg^{2+} as a cofactor (80–82), so we considered the possibility that UppS activity could be affected by altering the availability of Mg^{2+}. Although we do not exclude this possibility, several observations argue against it. First, *E. coli* UppS achieves maximal turnover (k_{cat}) around 0.5 mM $MgCl_2$ and half-maximal turnover at 49.0 μM $MgCl_2$ (80). The levels of labile, intracellular Mg^{2+} in *B. subtilis* (bulk measurements) are estimated to be between 0.8 and 3.7 mM in media containing 1.6 mM $MgCl_2$ (83). Notably, we still observe cell shortening at this concentration (Fig. 5). Thus, assuming that the *B. subtilis* and *E. coli* enzymes possess similar properties, there is likely sufficient Mg^{2+} to support full UppS activity when Mg^{2+} is not limiting the growth rate. Second, based on *in vitro* transcription termination measurements, the P_{mgtE} riboswitch transitions from an anti-terminator conformation to a terminator conformation between 2.0 and 3.0 mM Mg^{2+} (51). We did not see significant induction of the P_{mgtE}-*lacZ* reporter at the concentrations of Mg^{2+} at which the most dramatic changes in cell length were observed (Fig. 5C). This suggests that the pool of intracellular Mg^{2+} does not vary dramatically at the exogenous ranges that we focused on. Moreover, this is consistent with the observations made by others that intracellular Mg^{2+} does not vary significantly during exponential growth (83). Third, cell elongation also requires Und-P, and elongation was not affected in our conditions. Of course, it is possible that division is more sensitive to Und-P availability. At least in *E. coli*, there is some evidence that cells have a propensity to filament before bulging when Und-P is limiting (84). Finally, the rapid onset of division that we observed in the shifting experiment suggests that the cells have the capacity to divide without significant biosynthesis. Capturing these initial divisions in real time with a flow cell would provide more control and resolution regarding their timing.

One idea that is purely speculative is that the rapid division onset is driven by the more frequent flipping of Und-P to the cytoplasmic face of the membrane and/or the enhanced conversion of Und-PP to Und-P. There is also a pool of undecaprenyl-OH in some Gram-positives (85–88), so increasing Und-P availability through undecaprenyl-OH phosphorylation may be another route to enhancing pools. If the mechanism is not dependent on changes in cytoplasmic Mg^{2+} or on the activity of cytoplasmic enzymes such as UppS, there are also extracytoplasmic enzymes to consider. For example, the enzymes for wall teichoic acid and PG synthesis compete for Und-P, and there is at least one report that wall teichoic acid synthesis is favored over PG synthesis when Mg^{2+} is limited (89).

In summary, we show that the frequency of cell division can be uncoupled from the growth rate by manipulating a single nutrient, namely, Mg^{2+}. Though we did not arrive at a mechanism, we hope that the observations documented here will inspire further studies in additional bacteria as well as more consideration of medium selection during experimentation. Rich media are convenient but have the considerable weakness of variable formulation with regard to cofactor, trace metal, and amino acid abundance. Not only can this lead to confusing and irreproducible results but also (as we unintentionally discovered), rich media may be masking some important biology.

MATERIALS AND METHODS

General methods. The strains and the details of the strain construction can be found in the supplemental material (Table S4; Text S1). Cells were stored at −80°C in 15% glycerol (vol/vol). Strains were

streaked for isolation on lysogeny broth, Lennox (LB) containing 1.5% (wt/vol) bactoagar (Sigma) and were incubated overnight (approximately 16 h) at 37°C. Cultures for experiments were begun with colonies from same-day plates by inoculating single colonies into a 20 mm glass tube that contained 5 mL of the indicated medium. The tube was incubated at 37°C in a roller drum until the exponential stage ($OD_{600} < 0.6$). For the microscopy and RNA-seq experiments, the exponential-stage cultures (see above) were back-diluted in 25 mL of fresh medium in a 250 mL baffled flask to an optical density that would allow the cells to reach the desired growth stage (exponential) after no fewer than four doublings. The flasks were placed in a shaking water bath that was set to 280 rpm and 37°C.

The LB was made by dissolving 20 g of Difco LB Broth, Lennox (product number 240230) in 1 L ddH_2O, and this was followed by sterilization in an autoclave. The CH* utilized is a modified form of CH (49). The CH* (1L) contained 10.0 g casein acid hydrolysate (Acumedia, Lot No. 104,442B), 3.7 g L-glutamic acid (25.0 mM), 1.6 g L-asparagine monohydrate (10.0 mM), 1.25 g L-alanine (14.0 mM), 1.36 g (10.0 mM) anhydrous KH_2PO_4, 1.34 g (25.0 mM) NH_4Cl, 0.11 g Na_2SO_4 (0.77 mM), 0.1 g NH_4NO_3 (1.25 mM), 0.001 g $FeCl_3 \bullet 6H_2O$ (3.7 μM), and ddH_2O. The pH was adjusted to 7.0 with 10.0 N NaOH before the medium was sterilized in an autoclave. After autoclaving, sterile $CaCl_2$ was added to 0.2 mM, and L-sterile tryptophan was added to 0.1 mM. The base minimal medium (MM) contained 15.0 mM $(NH_4)_2SO_4$, 5.0 mM KH_2PO_4, 50.0 mM Tris-HCl [pH 7.5], 27.0 mM KCl, 0.05 mM $FeCl_3$, 0.01 mM $MnSO_2$, 0.01 mM $ZnSO_4$, 0.2% glucose (wt/vol), 27.0 mM sodium citrate, and 10.2 mM $CaCl_2$. 50.0 μM $MgCl_2$ was added to create the base medium used in the MM experiments, except for those in Fig. 5, which required final concentrations below 50.0 μM. In these experiments, $MgCl_2$ was added to the final concentrations indicated in the figure. For the MM-13aa, 10× filter-sterilized amino acids [pH 7.5] were added to a 1× final concentration. The 10× mixture consisted of the following concentrations of L-amino acids: 250.0 mM glutamate; 100.0 mM (each) alanine, asparagine, and proline; 50.0 mM (each) aspartic acid, phenylalanine, glycine, isoleucine, leucine, threonine, and valine; 10.0 mM (each) histidine and tryptophan. The amino acids were added to increase the growth rate but were selected based on their availability in our laboratory, not on logic.

***β*-galactosidase assays.** The *B. subtilis* strains were grown in 250 mL baffled flasks with 25 mL of the indicated medium at 37°C and 280 rpm to the target OD_{600}. The optical density was recorded, and 1 mL of culture was harvested via centrifugation at 21,130 × *g* for 1 min at room temperature, removing the supernatant via aspiration. The pellets were immediately stored at −80°C. To perform the assay, the pellets were thawed, resuspended in 0.5 mL Z-buffer (40.0 mM NaH_2PO_4, 60.0 mM Na_2HPO_4, 1.0 mM $MgSO_4$, 10.0 mM KCl, 40.0 mM β-mercaptoethanol, and 0.2 mg/mL lysozyme), and incubated at 30°C for 15 min. 100 μL of 4.0 mg/mL 2-nitrophenyl-β-D-galactopyranoside (ONPG) in Z-buffer was added, and the samples were incubated at 30°C until pale yellow. The reaction was stopped with 250 μL 1.0 M Na_2CO_3, and the reaction time was recorded. The sample was vortexed for 5 sec and centrifuged at 21,130 × *g* for 3 min at room temperature in a tabletop centrifuge. The supernatant (minimum volume of 0.8 mL) was transferred to a 1 mL cuvette, and the OD_{420} and OD_{550} absorbance readings were recorded. The β-galactosidase specific activity in Miller Units was calculated using the following formula: $(OD_{420} - [1.75\times OD_{550}]) / (\text{time [min]} \times \text{volume} \times OD_{600}) \times 1{,}000$.

Western blot analysis. 1 mL of culture was collected and spun at 21,130 × *g* for 1 min at room temperature at the exponential stage, and the OD_{600} value at the time of sampling was recorded. The pellet was resuspended in the lysis buffer (20.0 mM Tris [pH 7.5], 10.0 mM EDTA, 1 mg/mL lysozyme, 10 μg/mL DNase I, 100 μg/mL RNase A, 1.0 mM PMSF, 1 μL protease inhibitor cocktail [Sigma P8465-5ML] resuspended in 1 mL lysis buffer) to give a final OD_{600} equivalent of 15. The samples were incubated at 37°C for 10 min, and this was followed by the addition of an equal volume of sodium dodecyl sulfate (SDS) sample buffer (0.25 M Tris [pH 6.8], 4% [wt/vol] SDS, 20% [wt/vol], 20% glycerol [vol/vol], 10.0 mM EDTA, and 10% β-mercaptoethanol [vol/vol]). The samples were heated for 5 min at 100°C prior to loading. The proteins were separated on 12% SDS-PAGE polyacrylamide gels, transferred to a nitrocellulose membrane at 100 V for 60 min, and then blocked in 1× PBS containing 0.05% (vol/vol) Tween 20 and 5% (wt/vol) dry milk powder. The blocked membranes were probed overnight at 4°C with anti-SigA (1:20,000, rabbit, gift from Fujita Masaya, University of Houston, Houston, TX) diluted in 1× PBS with 0.05% (vol/vol) Tween 20 and 5% (wt/vol) milk powder. The membranes were washed three times with 1× PBS containing 0.05% (vol/vol) Tween 20, transferred to 1× PBS with 0.05% (vol/vol) Tween 20 and 5% (wt/vol) milk powder containing 1:5,000 horseradish peroxidase-conjugated goat anti-mouse IgG secondary antibodies (AbCam, ab205719), and incubated on a shaking platform for 1 h at room temperature. The membranes were washed 3× with 1× PBS containing 0.05% (vol/vol) Tween 20, and signals were detected using the SuperSignal West Femto Maximum Sensitivity Substrate (Thermo Fisher) and a Bio-Rad Gel Doc Imaging System.

Fluorescence microscopy. 1 mL of cultured cells at the exponential stage were harvested, concentrated via centrifugation at 6,010 × *g* for 1 min, and resuspended in 5 μL 1× PBS with either 1-(4-(trimethylamino) phenyl)-6-phenylhexa-1,3,5-triene (TMA-DPH) (50.0 μM) or N-(3-triethylammoniumpropyl)-4-(6-(4-(diethylamino) phenyl) hexatrienyl) pyridinium dibromide (FM4-64) (6 μg/mL) and 4′,6-diamidino-2-phenylindole (DAPI) (2 μg/mL). All dyes were purchased from Thermo Fisher. For the Zap-GFP and FtsZ-GFP experiments, the cells were mounted on 1% (wt/vol) agarose pads made with PBS [pH 7.4] and overlaid with an untreated glass coverslip. Otherwise, the cells were mounted on glass sides with poly-L-lysine-treated coverslips prior to imaging.

The cells were imaged on a Nikon Ti-E microscope using a CFI Plan Apo Lambda DM 100× objective and an X-Cite XYLIS 365 nm illumination system (Excelitas Technologies). The filter cubes utilized were C-FL UV-2E/C (DAPI), C-FL Texas Red HC HISN Zero Shift, and GFP HC HISN Zero Shift. Micrographs were acquired using a CoolSNAP HQ2 monochrome camera with NIS Elements Advanced Research, and they were analyzed in ImageJ (90).

Cell length measurements. The TMA-DPH micrographs were analyzed in ImageJ (90). For each cell, a line that extended from pole to pole was placed. One compartment between two bright, solid septa with homogenous signals were counted as one intact cell. Cells with bright partial septa or septa interrupted with discrete dark areas were counted as cells with partial septa.

Quantitation of Z-rings per unit cell length. The cell length lines (see above) were overlapped with the GFP micrographs of the Z-rings, and the number of Z-rings along the cell length line was counted. When two cells shared a pole and a Z-ring, each Z-ring was counted as 0.5/cell. The Z-ring number per μm was calculated by dividing the Z-ring total number by the total cell length.

Nucleoid number per cell. The cell length line was overlapped with the DAPI micrograph, and the cells were classified based on the number of nucleoids overlapping the length label. The number of nucleoids per cell was calculated by dividing the number of cells containing each number of nucleoids (1, 2, or 4) by the total number of cells counted.

Classification of septa in cells containing coalesced Z-rings. Micrographs of the GFP channel (ZapA-GFP or FtsZ-GFP) were overlaid with the corresponding TMA-DPH micrograph. The cells were classified as having no, partial, or full septa. The fraction of each septum type was determined by dividing the number of cells in each class by the total number of cells counted.

Statistical analysis and data plotting. The graphs were generated and the statistical analysis was performed using GraphPad Prism version 9.4.0 for Mac (GraphPad Software, San Diego, California, USA, www.graphpad.com). The statistical analyses in the following figures were performed via one-way analyses of variance (ANOVA) followed by Tukey's multiple-comparison tests, assuming Gaussian distributions with equal standard deviations (SDs): Fig. 3B, 5E, 6A, 6B, and 8B as well as Fig. S2B and S3C. The statistical analyses in the following figures were performed via two-way ANOVA followed by Tukey's multiple-comparison tests, fitting a full model: Fig. 7F and Fig. S3D. The statistical analyses in the following figures were performed via two-tailed unpaired *t* tests, assuming a Gaussian distribution and that both populations have the same SD: Fig. 1B, 2D, 6B, and 7E.

RNA-seq. For each condition, samples were collected from three independent biological replicates grown in either CH* medium or CH* medium with 10.0 mM $MgCl_2$. The cells were precultured in the same medium used for the experiment. 0.5 mL cells were collected at the exponential stage (OD_{600} ~of approximately 0.2) via centrifugation at 21,130 $\times$ *g* for 2 min at room temperature. RNA was collected using the RNAprotect Bacteria Reagent and an RNeasy Mini Kit (Qiagen) according to the manufacturer's instructions. RNA sequencing was performed by the Texas A&M AgriLife Research Genomics and Bioinformatics Service (College Station). The total RNA were prepared for sequencing using TruSeq Stranded Total RNA and Ribo-Zero Gold (Illumina). The RNA-seq was performed using a HISeq 4000 platform (Illumina). The RNA-seq data were processed through HISAT2 (91) and StringTie (92). A differential expression analysis was done using the Deseq2 R package (93). Regulons were assigned using the GinTool (62) starter package obtained from L.W. Hamoen (University of Amsterdam, Swammerdam Institute for Life Sciences). The cutoff for inclusion in the final analysis was set as genes with an absolute $\log_2$-fold change ($\log_2$FC) value of $\geq$0.585 and an adjusted *P*-value of $\leq$0.05. The adjusted *P*-values that are reported as 1.0 in the raw data indicate that the gene could not be included or excluded as statistically significant (generally due to insufficient reads in either the control or experimental samples).

Data availability. The raw RNA-seq data may be accessed through the NCBI Gene Expression Omnibus at the following link: https://www.ncbi.nlm.nih.gov/geo/query/acc.cgi?acc=GSE219221.

SUPPLEMENTAL MATERIAL

Supplemental material is available online only.

SUPPLEMENTAL FILE 1, PDF file, 13.4 MB.

SUPPLEMENTAL FILE 2, XLSX file, 0.8 MB.

ACKNOWLEDGMENTS

We thank Veronica Chemelewski for the critical reading of the manuscript, Morgan Chapman for the generation of the P_{hy}-*uppS* strain, Tatiana Castro Padovani for the assistance with visually screening deletion mutants for the loss of Mg^{2+}-responsiveness, and Leendert Hamoen for the sharing of the Gintool starter package. This work was supported by T. Guo teaching every semester and by scrap funds from the startup account of J.K. Herman. We dedicate this work to Ry Young in honor of his retirement.

REFERENCES

1. Jahnen-Dechent W, Ketteler M. 2012. Magnesium basics. Clin Kidney J 5:i3–i14. https://doi.org/10.1093/ndtplus/sfr163.
2. Sissi C, Palumbo M. 2009. Effects of magnesium and related divalent metal ions in topoisomerase structure and function. Nucleic Acids Res 37:702–711. https://doi.org/10.1093/nar/gkp024.
3. Meneely KM, Sundlov JA, Gulick AM, Moran GR, Lamb AL. 2016. An open and shut case: the interaction of magnesium with MST enzymes. J Am Chem Soc 138:9277–9293. https://doi.org/10.1021/jacs.6b05134.
4. Klein DJ, Moore PB, Steitz TA. 2004. The contribution of metal ions to the structural stability of the large ribosomal subunit. RNA 10:1366–1379. https://doi.org/10.1261/rna.7390804.
5. Akanuma G, Kobayashi A, Suzuki S, Kawamura F, Shiwa Y, Watanabe S, Yoshikawa H, Hanai R, Ishizuka M. 2014. Defect in the formation of 70S ribosomes caused by lack of ribosomal protein L34 can be suppressed by magnesium. J Bacteriol 196:3820–3830. https://doi.org/10.1128/JB.01896-14.

6. Pontes MH, Sevostyanova A, Groisman EA. 2015. When too much ATP is bad for protein synthesis. J Mol Biol 427:2586–2594. https://doi.org/10.1016/j.jmb.2015.06.021.
7. Bruna RE, Kendra CG, Groisman EA, Pontes MH. 2021. Limitation of phosphate assimilation maintains cytoplasmic magnesium homeostasis. Proc Natl Acad Sci U S A 118. https://doi.org/10.1073/pnas.2021370118.
8. Yin X, Wu Orr M, Wang H, Hobbs EC, Shabalina SA, Storz G. 2019. The small protein MgtS and small RNA MgrR modulate the PitA phosphate symporter to boost intracellular magnesium levels. Mol Microbiol 111:131–144. https://doi.org/10.1111/mmi.14143.
9. Wendel BM, Pi H, Kruger L, Herzberg C, Stulke J, Helmann JD. 2022. A central role for magnesium homeostasis during adaptation to osmotic stress. mBio 13:e0009222. https://doi.org/10.1128/mbio.00092-22.
10. de Melo JRF, Gutsch A, Caluwe T, Leloup JC, Gonze D, Hermans C, Webb AAR, Verbruggen N. 2021. Magnesium maintains the length of the circadian period in *Arabidopsis*. Plant Physiol 185:519–532. https://doi.org/10.1093/plphys/kiaa042.
11. Murray T, Popham DL, Setlow P. 1998. *Bacillus subtilis* cells lacking penicillin-binding protein 1 require increased levels of divalent cations for growth. J Bacteriol 180:4555–4563. https://doi.org/10.1128/JB.180.17.4555-4563.1998.
12. Matsuoka S, Chiba M, Tanimura Y, Hashimoto M, Hara H, Matsumoto K. 2011. Abnormal morphology of *Bacillus subtilis ugtP* mutant cells lacking glucolipids. Genes Genet Syst 86:295–304. https://doi.org/10.1266/ggs.86.295.
13. Schirner K, Errington J. 2009. The cell wall regulator σI specifically suppresses the lethal phenotype of *mbl* mutants in *Bacillus subtilis*. J Bacteriol 191:1404–1413. https://doi.org/10.1128/JB.01497-08.
14. Blaine J, Chonchol M, Levi M. 2015. Renal control of calcium, phosphate, and magnesium homeostasis. Clin J Am Soc Nephrol 10:1257–1272. https://doi.org/10.2215/CJN.09750913.
15. Moncany ML, Kellenberger E. 1981. High magnesium content of *Escherichia coli* B. Experientia 37:846–847. https://doi.org/10.1007/BF01985672.
16. Theillet FX, Binolfi A, Frembgen-Kesner T, Hingorani K, Sarkar M, Kyne C, Li C, Crowley PB, Gierasch L, Pielak GJ, Elcock AH, Gershenson A, Selenko P. 2014. Physicochemical properties of cells and their effects on intrinsically disordered proteins (IDPs). Chem Rev 114:6661–6714. https://doi.org/10.1021/cr400695p.
17. Alatossava T, Jutte H, Kuhn A, Kellenberger E. 1985. Manipulation of intracellular magnesium content in polymyxin B nonapeptide-sensitized *Escherichia coli* by ionophore A23187. J Bacteriol 162:413–419. https://doi.org/10.1128/jb.162.1.413-419.1985.
18. Tyrrell J, McGinnis JL, Weeks KM, Pielak GJ. 2013. The cellular environment stabilizes adenine riboswitch RNA structure. Biochemistry 52:8777–8785. https://doi.org/10.1021/bi401207q.
19. Outten CE, O'Halloran TV. 2001. Femtomolar sensitivity of metalloregulatory proteins controlling zinc homeostasis. Science 292:2488–2492. https://doi.org/10.1126/science.1060331.
20. Maguire ME, Cowan JA. 2002. Magnesium chemistry and biochemistry. Biometals 15:203–210. https://doi.org/10.1023/a:1016058229972.
21. Pontes MH, Yeom J, Groisman EA. 2016. Reducing ribosome biosynthesis promotes translation during low Mg(2+) stress. Mol Cell 64:480–492. https://doi.org/10.1016/j.molcel.2016.05.008.
22. Groisman EA. 2001. The pleiotropic two-component regulatory system PhoP-PhoQ. J Bacteriol 183:1835–1842. https://doi.org/10.1128/JB.183.6.1835-1842.2001.
23. Groisman EA, Duprey A, Choi J. 2021. How the PhoP/PhoQ system controls virulence and Mg(2+) homeostasis: lessons in signal transduction, pathogenesis, physiology, and evolution. Microbiol Mol Biol Rev 85:e0017620. https://doi.org/10.1128/MMBR.00176-20.
24. Wakeman CA, Goodson JR, Zacharia VM, Winkler WC. 2014. Assessment of the requirements for magnesium transporters in *Bacillus subtilis*. J Bacteriol 196:1206–1214. https://doi.org/10.1128/JB.01238-13.
25. Krom BP, Warner JB, Konings WN, Lolkema JS. 2000. Complementary metal ion specificity of the metal-citrate transporters CitM and CitH of *Bacillus subtilis*. J Bacteriol 182:6374–6381. https://doi.org/10.1128/JB.182.22.6374-6381.2000.
26. Krom BP, Huttinga H, Warner JB, Lolkema JS. 2002. Impact of the Mg(2+)-citrate transporter CitM on heavy metal toxicity in *Bacillus subtilis*. Arch Microbiol 178:370–375. https://doi.org/10.1007/s00203-002-0465-8.
27. Smith RL, Maguire ME. 1998. Microbial magnesium transport: unusual transporters searching for identity. Mol Microbiol 28:217–226. https://doi.org/10.1046/j.1365-2958.1998.00810.x.
28. Rogers HJ, Thurman PF, Buxton RS. 1976. Magnesium and anion requirements of *rodB* mutants of *Bacillus subtilis*. J Bacteriol 125:556–564. https://doi.org/10.1128/jb.125.2.556-564.1976.
29. Kawai Y, Asai K, Errington J. 2009. Partial functional redundancy of MreB isoforms, MreB, Mbl and MreBH, in cell morphogenesis of *Bacillus subtilis*. Mol Microbiol 73:719–731. https://doi.org/10.1111/j.1365-2958.2009.06805.x.
30. Leaver M, Errington J. 2005. Roles for MreC and MreD proteins in helical growth of the cylindrical cell wall in *Bacillus subtilis*. Mol Microbiol 57:1196–1209. https://doi.org/10.1111/j.1365-2958.2005.04736.x.
31. Carballido-Lopez R, Formstone A, Li Y, Ehrlich SD, Noirot P, Errington J. 2006. Actin homolog MreBH governs cell morphogenesis by localization of the cell wall hydrolase LytE. Dev Cell 11:399–409. https://doi.org/10.1016/j.devcel.2006.07.017.
32. Wagner PM, Stewart GC. 1991. Role and expression of the *Bacillus subtilis rodC* operon. J Bacteriol 173:4341–4346. https://doi.org/10.1128/jb.173.14.4341-4346.1991.
33. Lazarevic V, Soldo B, Medico N, Pooley H, Bron S, Karamata D. 2005. *Bacillus subtilis* alpha-phosphoglucomutase is required for normal cell morphology and biofilm formation. Appl Environ Microbiol 71:39–45. https://doi.org/10.1128/AEM.71.1.39-45.2005.
34. Gorke B, Foulquier E, Galinier A. 2005. YvcK of *Bacillus subtilis* is required for a normal cell shape and for growth on Krebs cycle intermediates and substrates of the pentose phosphate pathway. Microbiology (Reading) 151:3777–3791. https://doi.org/10.1099/mic.0.28172-0.
35. Wecke J, Madela K, Fischer W. 1997. The absence of D-alanine from lipoteichoic acid and wall teichoic acid alters surface charge, enhances autolysis and increases susceptibility to methicillin in *Bacillus subtilis*. Microbiology (Reading) 143:2953–2960. https://doi.org/10.1099/00221287-143-9-2953.
36. Dajkovic A, Tesson B, Chauhan S, Courtin P, Keary R, Flores P, Marliere C, Filipe SR, Chapot-Chartier MP, Carballido-Lopez R. 2017. Hydrolysis of peptidoglycan is modulated by amidation of meso-diaminopimelic acid and Mg(2+) in *Bacillus subtilis*. Mol Microbiol 104:972–988. https://doi.org/10.1111/mmi.13673.
37. Tesson B, Dajkovic A, Keary R, Marliere C, Dupont-Gillain CC, Carballido-Lopez R. 2022. Magnesium rescues the morphology of *Bacillus subtilis mreB* mutants through its inhibitory effect on peptidoglycan hydrolases. Sci Rep 12:1137. https://doi.org/10.1038/s41598-021-04294-5.
38. Christensen DG, Orr JS, Rao CV, Wolfe AJ. 2017. Increasing growth yield and decreasing acetylation in *Escherichia coli* by optimizing the carbon-to-magnesium ratio in peptide-based media. Appl Environ Microbiol 83. https://doi.org/10.1128/AEM.03034-16.
39. Webb M. 1951. The influence of magnesium on cell division. IV. The specificity of magnesium. J Gen Microbiol 5:480–484. https://doi.org/10.1099/00221287-5-3-480.
40. Webb M. 1951. The influence of magnesium on cell division. V. The effect of magnesium on the growth of bacteria in chemically-defined media of varying complexity. J Gen Microbiol 5:485–495. https://doi.org/10.1099/00221287-5-3-485.
41. Webb M. 1951. The influence of magnesium on cell division. VI. The action of certain hydrolytic enzymes on the filamentous and chain forms of gram-positive rod-shaped organisms. J Gen Microbiol 5:496–501. https://doi.org/10.1099/00221287-5-3-496.
42. Yaginuma H, Kawai S, Tabata KV, Tomiyama K, Kakizuka A, Komatsuzaki T, Noji H, Imamura H. 2014. Diversity in ATP concentrations in a single bacterial cell population revealed by quantitative single-cell imaging. Sci Rep 4:6522. https://doi.org/10.1038/srep06522.
43. Westfall CS, Levin PA. 2018. Comprehensive analysis of central carbon metabolism illuminates connections between nutrient availability, growth rate, and cell morphology in *Escherichia coli*. PLoS Genet 14:e1007205. https://doi.org/10.1371/journal.pgen.1007205.
44. Vadia S, Tse JL, Lucena R, Yang Z, Kellogg DR, Wang JD, Levin PA. 2017. Fatty acid availability sets cell envelope capacity and dictates microbial cell size. Curr Biol 27:1757–1767. https://doi.org/10.1016/j.cub.2017.05.076.
45. Taheri-Araghi S, Bradde S, Sauls JT, Hill NS, Levin PA, Paulsson J, Vergassola M, Jun S. 2015. Cell-size control and homeostasis in bacteria. Curr Biol 25:385–391. https://doi.org/10.1016/j.cub.2014.12.009.
46. Sargent MG. 1975. Control of cell length in *Bacillus subtilis*. J Bacteriol 123:7–19. https://doi.org/10.1128/jb.123.1.7-19.1975.
47. Vadia S, Levin PA. 2015. Growth rate and cell size: a re-examination of the growth law. Curr Opin Microbiol 24:96–103. https://doi.org/10.1016/j.mib.2015.01.011.
48. Schaechter M, Maaloe O, Kjeldgaard NO. 1958. Dependency on medium and temperature of cell size and chemical composition during balanced

grown of *Salmonella typhimurium*. J Gen Microbiol 19:592–606. https://doi.org/10.1099/00221287-19-3-592.
49. Sterlini JM, Mandelstam J. 1969. Commitment to sporulation in *Bacillus subtilis* and its relationship to development of actinomycin resistance. Biochem J 113:29–37. https://doi.org/10.1042/bj1130029.
50. Zeigler DR, Pragai Z, Rodriguez S, Chevreux B, Muffler A, Albert T, Bai R, Wyss M, Perkins JB. 2008. The origins of 168, W23, and other *Bacillus subtilis* legacy strains. J Bacteriol 190:6983–6995. https://doi.org/10.1128/JB.00722-08.
51. Dann CE, 3rd, Wakeman CA, Sieling CL, Baker SC, Irnov I, Winkler WC. 2007. Structure and mechanism of a metal-sensing regulatory RNA. Cell 130:878–892. https://doi.org/10.1016/j.cell.2007.06.051.
52. Ramesh A, Winkler WC. 2010. Magnesium-sensing riboswitches in bacteria. RNA Biol 7:77–83. https://doi.org/10.4161/rna.7.1.10490.
53. Pi H, Wendel BM, Helmann JD. 2020. Dysregulation of magnesium transport protects *Bacillus subtilis* against manganese and cobalt intoxication. J Bacteriol 202. https://doi.org/10.1128/JB.00711-19.
54. Gamba P, Veening JW, Saunders NJ, Hamoen LW, Daniel RA. 2009. Two-step assembly dynamics of the *Bacillus subtilis* divisome. J Bacteriol 191:4186–4194. https://doi.org/10.1128/JB.01758-08.
55. Gueiros-Filho FJ, Losick R. 2002. A widely conserved bacterial cell division protein that promotes assembly of the tubulin-like protein FtsZ. Genes Dev 16:2544–2556. https://doi.org/10.1101/gad.1014102.
56. Garrett AJ. 1969. The effect of magnesium ion deprivation on the synthesis of mucopeptide and its precursors in *Bacillus subtilis*. Biochem J 115:419–430. https://doi.org/10.1042/bj1150419.
57. Bouhss A, Crouvoisier M, Blanot D, Mengin-Lecreulx D. 2004. Purification and characterization of the bacterial MraY translocase catalyzing the first membrane step of peptidoglycan biosynthesis. J Biol Chem 279:29974–29980. https://doi.org/10.1074/jbc.M314165200.
58. Radeck J, Lautenschlager N, Mascher T. 2017. The Essential UPP phosphatase pair BcrC and UppP connects cell wall homeostasis during growth and sporulation with cell envelope stress response in *Bacillus subtilis*. Front Microbiol 8:2403. https://doi.org/10.3389/fmicb.2017.02403.
59. Bernard R, El Ghachi M, Mengin-Lecreulx D, Chippaux M, Denizot F. 2005. BcrC from *Bacillus subtilis* acts as an undecaprenyl pyrophosphate phosphatase in bacitracin resistance. J Biol Chem 280:28852–28857. https://doi.org/10.1074/jbc.M413750200.
60. Inaoka T, Ochi K. 2012. Undecaprenyl pyrophosphate involvement in susceptibility of *Bacillus subtilis* to rare earth elements. J Bacteriol 194:5632–5637. https://doi.org/10.1128/JB.01147-12.
61. Pedreira T, Elfmann C, Stulke J. 2022. The current state of SubtiWiki, the database for the model organism *Bacillus subtilis*. Nucleic Acids Res 50:D875–D882. https://doi.org/10.1093/nar/gkab943.
62. FvdK BW, Kes MB, Luirink J, Hamoen LW. 2022. Transcriptome analyses using regulon, functional category, and operon information with GINtool. Biorxiv. https://doi.org/10.1101/2022.10.24.513545.
63. Serizawa M, Kodama K, Yamamoto H, Kobayashi K, Ogasawara N, Sekiguchi J. 2005. Functional analysis of the YvrGHb two-component system of *Bacillus subtilis*: identification of the regulated genes by DNA microarray and northern blot analyses. Biosci Biotechnol Biochem 69:2155–2169. https://doi.org/10.1271/bbb.69.2155.
64. Nikaido H. 2009. Small things considered: the limitations of LB medium. https://schaechter.asmblog.org/schaechter/2009/11/the-limitations-of-lb-medium.html.
65. Volland JM, Gonzalez-Rizzo S, Gros O, Tyml T, Ivanova N, Schulz F, Goudeau D, Elisabeth NH, Nath N, Udwary D, Malmstrom RR, Guidi-Rontani C, Bolte-Kluge S, Davies KM, Jean MR, Mansot JL, Mouncey NJ, Angert ER, Woyke T, Date SV. 2022. A centimeter-long bacterium with DNA contained in metabolically active, membrane-bound organelles. Science 376:1453–1458. https://doi.org/10.1126/science.abb3634.
66. Larkin JM, Strohl WR. 1983. Beggiatoa, Thiothrix, and Thioploca. Annu Rev Microbiol 37:341–367. https://doi.org/10.1146/annurev.mi.37.100183.002013.
67. Newman EB, Budman LI, Chan EC, Greene RC, Lin RT, Woldringh CL, D'Ari R. 1998. Lack of S-adenosylmethionine results in a cell division defect in *Escherichia coli*. J Bacteriol 180:3614–3619. https://doi.org/10.1128/JB.180.14.3614-3619.1998.
68. Winterbourn CC. 1995. Toxicity of iron and hydrogen peroxide: the Fenton reaction. Toxicol Lett 82–83:969–974. https://doi.org/10.1016/0378-4274(95)03532-x.
69. Aguirre JD, Culotta VC. 2012. Battles with iron: manganese in oxidative stress protection. J Biol Chem 287:13541–13548. https://doi.org/10.1074/jbc.R111.312181.
70. MacCain WJ, Kannan S, Jameel DZ, Troutman JM, Young KD. 2018. A defective undecaprenyl pyrophosphate synthase induces growth and morphological defects that are suppressed by mutations in the isoprenoid pathway of *Escherichia coli*. J Bacteriol 200. https://doi.org/10.1128/JB.00255-18.
71. Gaballa A, Helmann JD. 2002. A peroxide-induced zinc uptake system plays an important role in protection against oxidative stress in *Bacillus subtilis*. Mol Microbiol 45:997–1005. https://doi.org/10.1046/j.1365-2958.2002.03068.x.
72. Murdoch CC, Skaar EP. 2022. Nutritional immunity: the battle for nutrient metals at the host-pathogen interface. Nat Rev Microbiol 20:657–670. https://doi.org/10.1038/s41579-022-00745-6.
73. Si M, Zhao C, Burkinshaw B, Zhang B, Wei D, Wang Y, Dong TG, Shen X. 2017. Manganese scavenging and oxidative stress response mediated by type VI secretion system in *Burkholderia thailandensis*. Proc Natl Acad Sci U S A 114:E2233–E2242.
74. Inaoka T, Matsumura Y, Tsuchido T. 1999. SodA and manganese are essential for resistance to oxidative stress in growing and sporulating cells of *Bacillus subtilis*. J Bacteriol 181:1939–1943. https://doi.org/10.1128/JB.181.6.1939-1943.1999.
75. Eide DJ. 2011. The oxidative stress of zinc deficiency. Metallomics 3:1124–1129. https://doi.org/10.1039/c1mt00064k.
76. Arjes HA, Vo L, Dunn CM, Willis L, DeRosa CA, Fraser CL, Kearns DB, Huang KC. 2020. Biosurfactant-mediated membrane depolarization maintains viability during oxygen depletion in *Bacillus subtilis*. Curr Biol 30:1011–1022. https://doi.org/10.1016/j.cub.2020.01.073.
77. Rodriguez Ayala F, Bartolini M, Grau R. 2020. The stress-responsive alternative sigma factor SigB of *Bacillus subtilis* and its relatives: an old friend with new functions. Front Microbiol 11:1761. https://doi.org/10.3389/fmicb.2020.01761.
78. Nicolas P, Mader U, Dervyn E, Rochat T, Leduc A, Pigeonneau N, Bidnenko E, Marchadier E, Hoebeke M, Aymerich S, Becher D, Bisicchia P, Botella E, Delumeau O, Doherty G, Denham EL, Fogg MJ, Fromion V, Goelzer A, Hansen A, Hartig E, Harwood CR, Homuth G, Jarmer H, Jules M, Klipp E, Le Chat L, Lecointe F, Lewis P, Liebermeister W, March A, Mars RA, Nannapaneni P, Noone D, Pohl S, Rinn B, Rugheimer F, Sappa PK, Samson F, Schaffer M, Schwikowski B, Steil L, Stulke J, Wiegert T, Devine KM, Wilkinson AJ, van Dijl JM, Hecker M, Volker U, Bessieres P, et al. 2012. Condition-dependent transcriptome reveals high-level regulatory architecture in *Bacillus subtilis*. Science 335:1103–1106. https://doi.org/10.1126/science.1206848.
79. Ng W. 2021. Categorization of prophage genes in *Bacillus subtilis* 168 and assessing their relative importance through RNA-seq gene expression analysis. Biorxiv. https://www.biorxiv.org/content/10.1101/2021.10.26.466030v1.
80. Guo RT, Ko TP, Chen AP, Kuo CJ, Wang AH, Liang PH. 2005. Crystal structures of undecaprenyl pyrophosphate synthase in complex with magnesium, isopentenyl pyrophosphate, and farnesyl thiopyrophosphate: roles of the metal ion and conserved residues in catalysis. J Biol Chem 280:20762–20774. https://doi.org/10.1074/jbc.M502121200.
81. Chang SY, Ko TP, Chen AP, Wang AH, Liang PH. 2004. Substrate binding mode and reaction mechanism of undecaprenyl pyrophosphate synthase deduced from crystallographic studies. Protein Sci 13:971–978. https://doi.org/10.1110/ps.03519904.
82. Chang SY, Ko TP, Liang PH, Wang AH. 2003. Catalytic mechanism revealed by the crystal structure of undecaprenyl pyrophosphate synthase in complex with sulfate, magnesium, and triton. J Biol Chem 278:29298–29307. https://doi.org/10.1074/jbc.M302687200.
83. McCluskey K, Boudreault J, St-Pierre P, Perez-Gonzalez C, Chauvier A, Rizzi A, Beauregard PB, Lafontaine DA, Penedo JC. 2019. Unprecedented tunability of riboswitch structure and regulatory function by sub-millimolar variations in physiological Mg2. Nucleic Acids Res 47:6478–6487. https://doi.org/10.1093/nar/gkz316.
84. Jorgenson MA, Kannan S, Laubacher ME, Young KD. 2016. Dead-end intermediates in the enterobacterial common antigen pathway induce morphological defects in *Escherichia coli* by competing for undecaprenyl phosphate. Mol Microbiol 100:1–14. https://doi.org/10.1111/mmi.13284.
85. Barreteau H, Magnet S, El Ghachi M, Touze T, Arthur M, Mengin-Lecreulx D, Blanot D. 2009. Quantitative high-performance liquid chromatography analysis of the pool levels of undecaprenyl phosphate and its derivatives in bacterial membranes. J Chromatogr B Analyt Technol Biomed Life Sci 877:213–220. https://doi.org/10.1016/j.jchromb.2008.12.010.
86. Higashi Y, Siewert G, Strominger JL. 1970. Biosynthesis of the peptidoglycan of bacterial cell walls. XIX. Isoprenoid alcohol phosphokinase. J Biol Chem 245:3683–3690. https://doi.org/10.1016/S0021-9258(18)62980-1.

87. Gough DP, Kirby AL, Richards JB, Hemming FW. 1970. The characterization of undecaprenol of *Lactobacillus plantarum*. Biochem J 118:167–170. https://doi.org/10.1042/bj1180167.
88. Umbreit JN, Stone KJ, Strominger JL. 1972. Isolation of polyisoprenyl alcohols from *Streptococcus faecalis*. J Bacteriol 112:1302–1305. https://doi.org/10.1128/jb.112.3.1302-1305.1972.
89. Anderson RG, Hussey H, Baddiley J. 1972. The mechanism of wall synthesis in bacteria. The organization of enzymes and isoprenoid phosphates in the membrane. Biochem J 127:11–25. https://doi.org/10.1042/bj1270011.
90. Rasband WS. 1997. 2018. ImageJ, U.S. National Institutes of Health, Bethesda, Maryland. USA. https://imagej.nih.gov/ij/.
91. Kim D, Paggi JM, Park C, Bennett C, Salzberg SL. 2019. Graph-based genome alignment and genotyping with HISAT2 and HISAT-genotype. Nat Biotechnol 37:907–915. https://doi.org/10.1038/s41587-019-0201-4.
92. Pertea M, Pertea GM, Antonescu CM, Chang TC, Mendell JT, Salzberg SL. 2015. StringTie enables improved reconstruction of a transcriptome from RNA-seq reads. Nat Biotechnol 33:290–295. https://doi.org/10.1038/nbt.3122.
93. Love MI, Huber W, Anders S. 2014. Moderated estimation of fold change and dispersion for RNA-seq data with DESeq2. Genome Biol 15:550. https://doi.org/10.1186/s13059-014-0550-8.

Supplementary materials

Magnesium modulates *Bacillus subtilis* cell division frequency

Tingfeng Guo and J.K. Herman*

Short title: Mg^{2+} effects cell division

Department of Biochemistry and Biophysics, Texas A&M University, College Station, TX

Corresponding author*

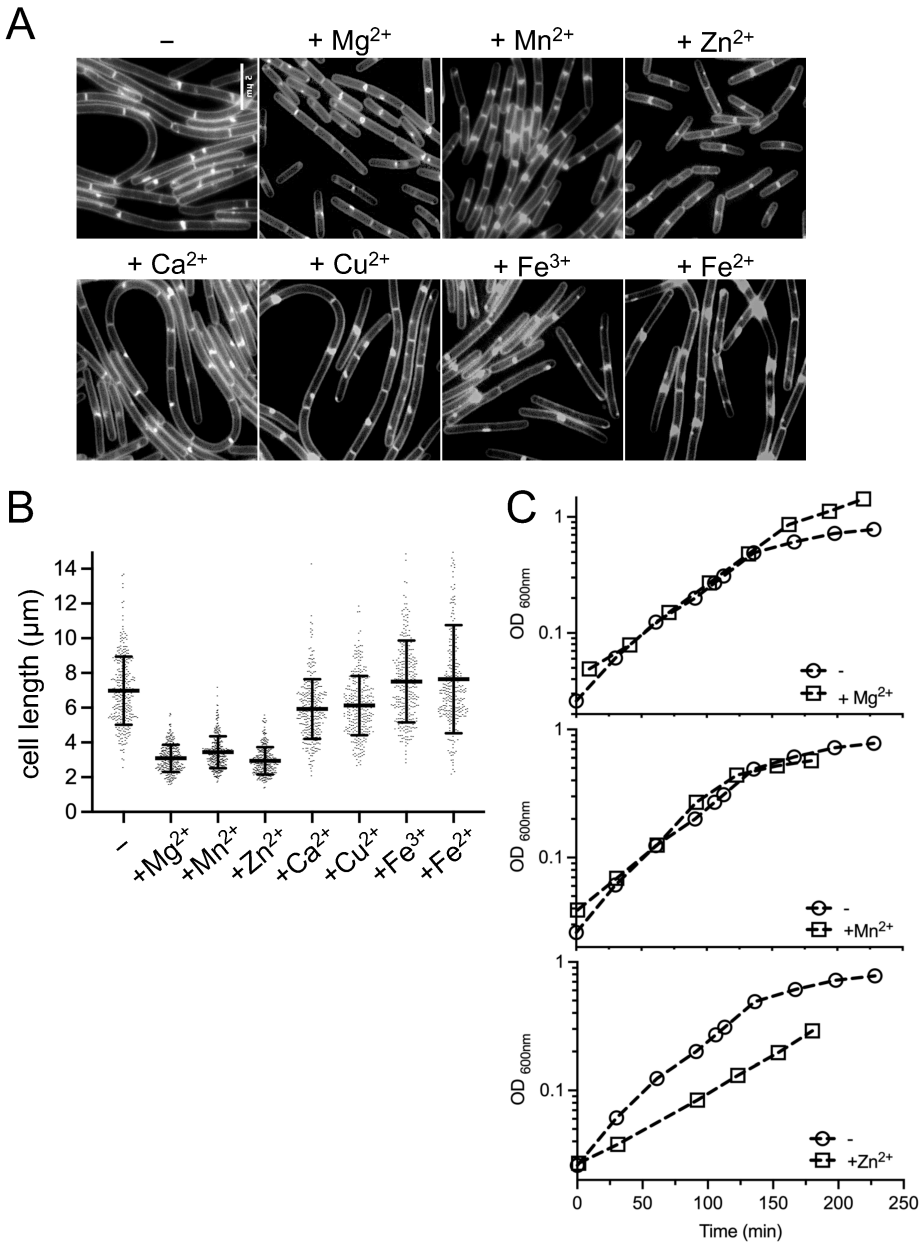

Figure S1. Effect of divalent metals on cell length. Wild-type 168 (BJH004) cells were cultured in CH* and, when indicated, the following concentrations of divalent cation salts: 10.0 mM $MgCl_2$, 0.1 mM $MnSO_4$, 0.2 mM $ZnCl_2$, 1.0 mM $CaCl_2$, 0.5 mM $CuSO_4$, 0.1 mM $Fe_2(SO_4)_3$, and 0.5 mM $FeSO_4$. (A) Micrographs following membrane staining and epifluorescent microscopy (scaled identically). (B) Scatter plots showing the distribution of cell lengths quantitated for 300 cells from each condition. Bars represent the means of 300 cells ± SD. The data for Mg^{2+}, Mn^{2+}, and Zn^{2+} are the same as shown in Figure 3. (C) Representative growth curves.

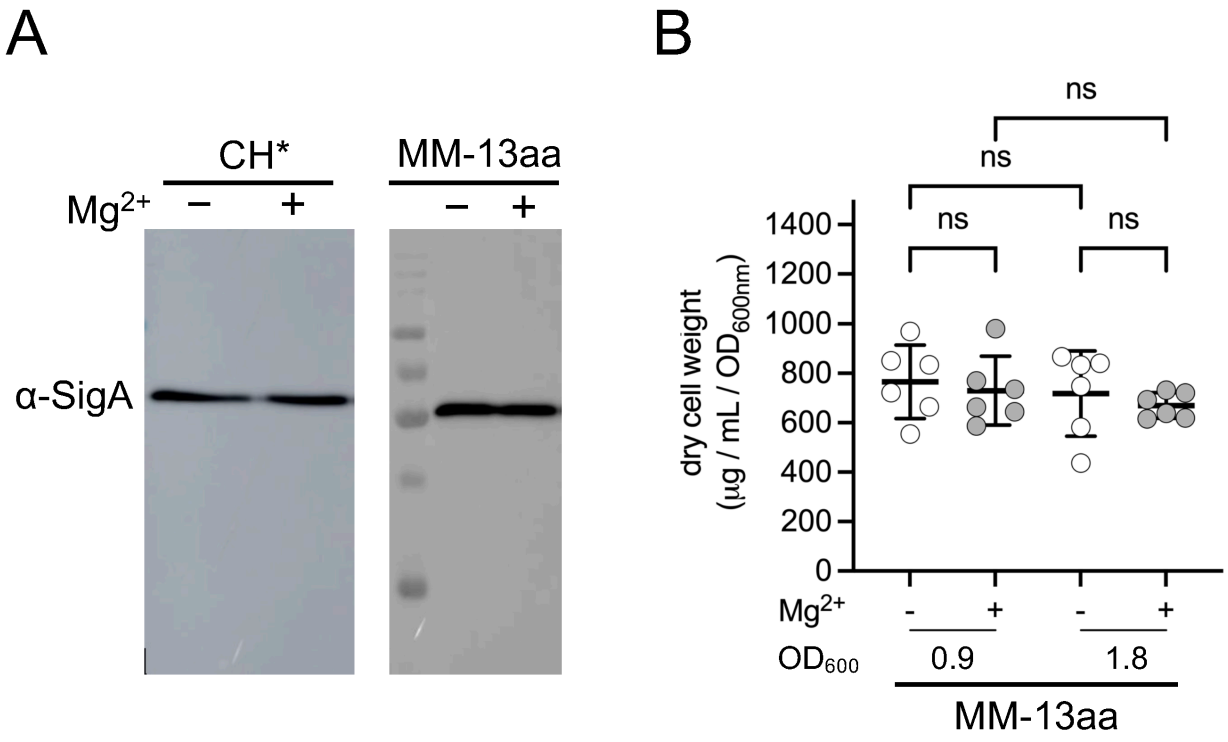

Figure S2. Controls assessing the robustness OD_{600} reading as a measurement of growth. (A) Immunoblot analysis of SigA expression level of *B. subtilis* 168 (BJH004) cells grown in CH* or MM-13aa. 10.0 mM $MgCl_2$ was added as indicated. Cells were harvested at OD_{600} of ~0.2 and sample loads were normalized to each other using OD_{600} values. (B) Dry cell weight of *B. subtilis* 168 (BJH004) cultured in MM-13aa. 10.0 mM $MgCl_2$ was added as indicated. Growth is still linear at an OD_{600} of 0.9 in MM-13aa (see Fig 3A). (ns) $p \geq 0.05$.

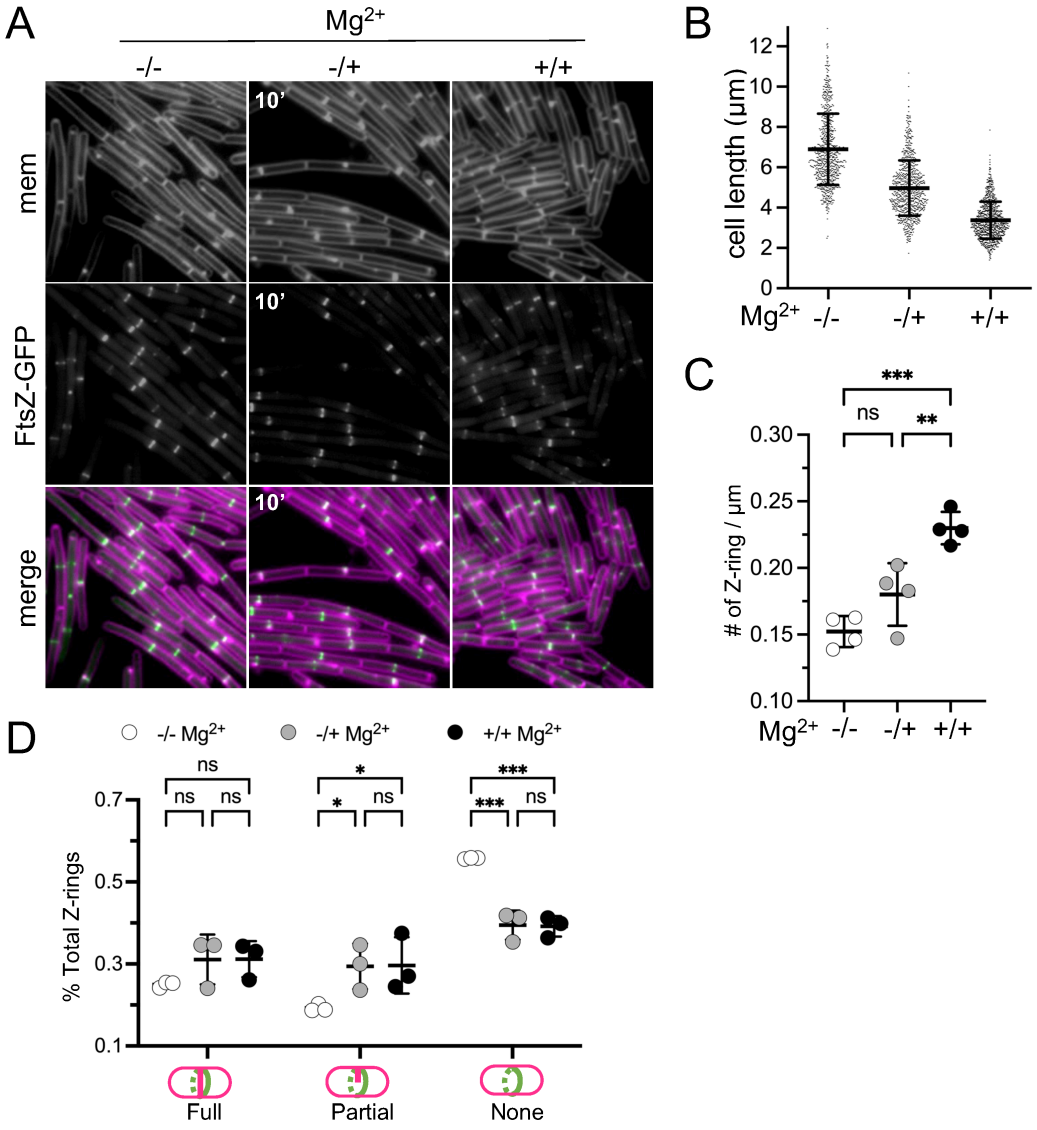

Figure S3. Imaging and quantitation of FtsZ-GFP following Mg2+ supplementation. P*spac*-*ftsZ-GFP* (BTG185) was grown in MM-13aa with 5.0 µM IPTG. For the transfer experiment, cells were imaged 10 min after the addition of 10.0 mM $MgCl_2$ (-/+). (A) Representative micrographs. Membranes stained with FM4-64. (B) Scatter plots showing the distribution of cell lengths. Bars represent the mean cell lengths 800 cells ± SD. (C) Average number of Z-rings per unit cell length ± SD. Each circle represents the mean of 200 cells from four independent biological replicates per condition. (D) Average fraction of cells with coalesced FtsZ-GFP presenting the indicated septum type ± SD. Each circle represents the mean of 500 cells from three independent biological replicates per condition. (***) $0.0001<p\leq0.001$, (**) $0.001<p\leq0.01$, (*) $0.01<p\leq0.05$, (ns) $p\geq0.05$.

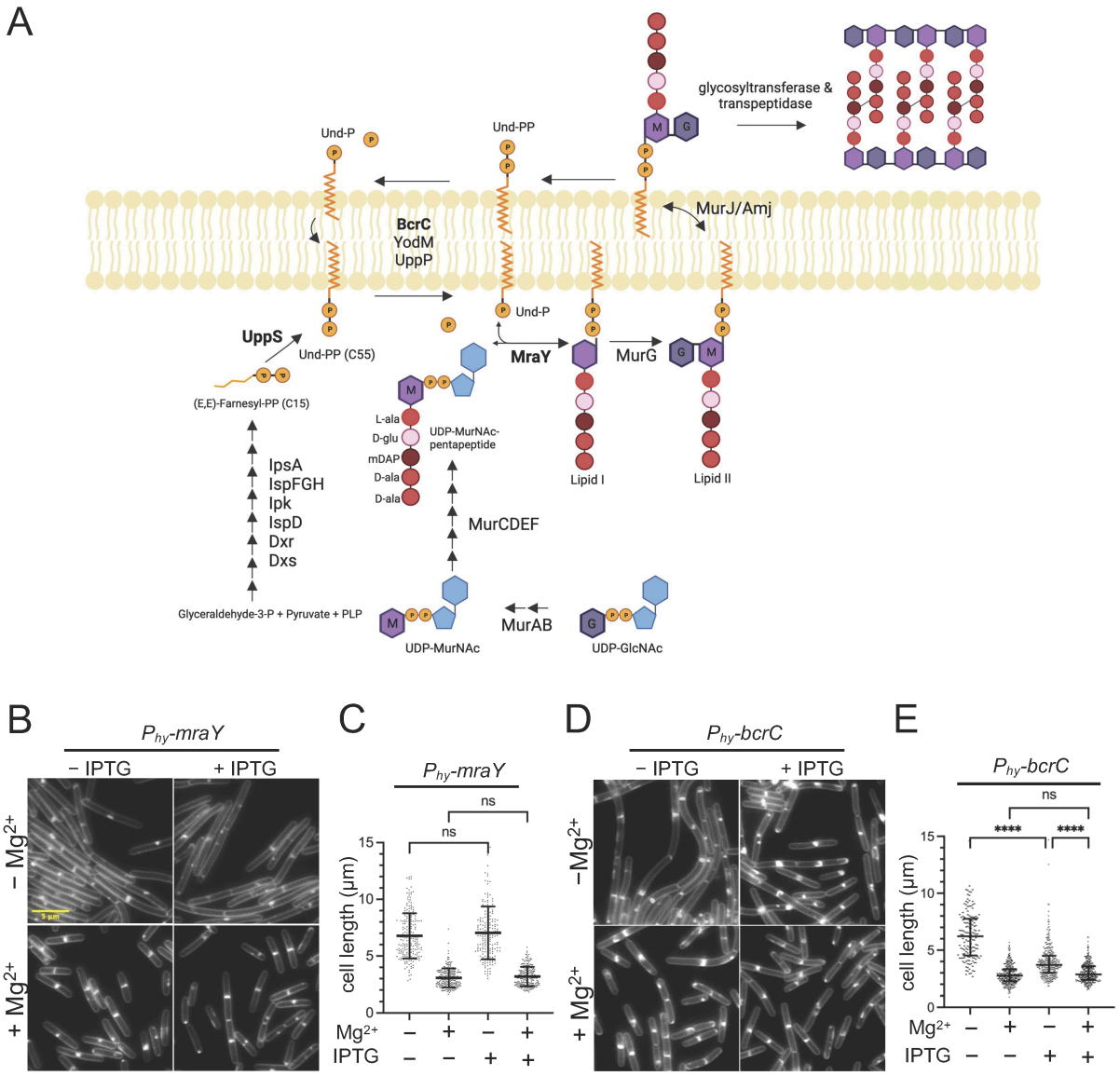

Figure S4. (A) Peptidoglycan biosynthesis pathway. Representative micrographs of (B) *P*$_{hy}$*-mraY* (BTG697) and (D) *P*$_{hy}$*-bcrC* (BTG678) cultured in CH* with 1.0 mM IPTG, with or without 10.0 mM $MgCl_2$. Membranes are stained with TMA and images are scaled identically. (C and E) scatter plots showing the distribution of cell lengths quantitated for 150 cells from each condition. Bars represent the mean cell length ± SD. (****) $p<0.0001$, (ns) $p>0.05$.

Table S1. RNA-seq analysis of genes upregulated in (CH$^+$ + 10.0 mM $MgCl_2$)/(CH$^+$).

Fold-change	Gene ID	Gene	Description	Regulon									Deletion strain Mg2+ responsive?
9.2	BSU_14150	ykoW	replaces fumarylpyruvate under conditions of iron limitation	Fur	Kre	ResD	NsrR				SigI	SigA	N/A
9.1	BSU_14160	ykoV	unknown	Fur	Kre	ResD	NsrR				SigI	SigA	N/A
9.0	BSU_14170	ykoP	replaces fumarylpyruvate under conditions of iron limitation	Fur	Kre	ResD	NsrR				SigI	SigA	N/A
8.6	BSU_31954	dhbG	unknown	Fur	Kre			AbrB			SigI	SigA	N/A
8.6	BSU_31960	dhbF	biosynthesis of the siderophore bacillibactin	Fur	Kre			AbrB			SigI	SigA	N/A
8.6	BSU_31970	dhbB		Fur	Kre			AbrB			SigI	SigA	+
8.1	BSU_31980	dhbE		Fur	Kre			AbrB			SigI	SigA	+
8.0	BSU_31990	dhbC		Fur	Kre			AbrB			SigI	SigA	+
8.0	BSU_32000	dhbA		Fur	Kre			AbrB			SigI	SigA	+
6.4	BSU_01630	feuA	ABC transporter for the siderophores	Fur	Bir							SigA	N/A
4.9	BSU_01610	feuC		Fur	Bir							SigA	N/A
4.9	BSU_01620	feuB		Fur	Bir							SigA	N/A
4.5	BSU_01600	pbtA	release of iron from enterobactin	Fur	Bir							sigA	N/A
4.3	BSU_04534	fhpA	Acquisition of iron	Fur									N/A
4.1	BSU_04530	fhpB		Fur									N/A
3.7	BSU_32010	bacA		Fur				AbrB					N/A
3.5	BSU_39610	yvmB	siderophore uptake	Fur									N/A
3.3	BSU_07150	hmuA	heme microorganisms	Fur									N/A
3.2	BSU_07320	lmrC	iron uptake	Fur									N/A
1.9	BSU_10330	yfhQ		Fur									N/A
2.1	BSU_03290	fhuC	siderophore uptake	Fur									N/A
2.1	BSU_03300	fhuB		Fur									N/A
1.9	BSU_03310	fhuD		Fur									N/A
1.8	BSU_03320	fhuG		Fur							SigB		N/A
2.1	BSU_07230	yqjB	unknown	Fur							SigB		N/A
1.8	BSU_07220	yqjM		Fur							SigB		N/A
1.5	BSU_39260	efeU	elemental iron uptake system	Fur					SigX	SigM	SigM	SigA	N/A
1.6	BSU_39270	efeO		Fur					SigX	SigM	SigM	SigA	N/A
1.5	BSU_39280	efeA		Fur					SigX	SigM	SigM	SigA	N/A
1.6	BSU_08440	yfiY	acquisition of iron	Fur									N/A
1.5	BSU_06230	cotJC	essential for this viability in the presence of catechol	Fur	CatR	YvaB						SigA	N/A
1.3	BSU_08240	cotE		Fur	CatR	YvaB						SigA	N/A
1.5	BSU_03830	bdcO	petrobactin acquisition of iron	Fur									N/A
1.3	BSU_03810	bpsD		Fur									N/A
1.3	BSU_03800	bpsA		Fur									N/A
1.6	BSU_01640	sfp	regulation of iron acquisition	Fur									N/A
10.1	BSU_03350	yhfL	unknown	Zur								SigA	N/A
2.6	BSU_30700	ganAB	replaces RpmE under conditions of zinc limitation	Zur							SigB		N/A
1.9	BSU_08860	ganAB	replaces RpsN under conditions of zinc limitation	Zur	YtaR								N/A
1.3	BSU_06830	zinT	lipoprotein, similar to zinc-binding protein	Zur								SigA	N/A
6.8	BSU_30750	zosC	manganese uptake	MntR									N/A
6.3	BSU_30760	zosB		MntR									N/A
6.1	BSU_30770	zosA		MntR									+
5.8	BSU_30740	zosD		MntR									+
2.4	BSU_06360	zosE		MntR									N/A
2.5	BSU_03460	sdrA	surfactin synthetase / competence	PerR	CodY	ComA	Spx	Abh	PhoP			SigA	+
2.6	BSU_03490	sdrA5		PerR	CodY	ComA	Spx	Abh	PhoP			SigA	+
2.6	BSU_03520	sdrA3		PerR	CodY	ComA	Spx	Abh	PhoP			SigA	N/A
2.6	BSU_03510	sdrA2		PerR	CodY	ComA	Spx	Abh	PhoP			SigA	+
4.9	BSU_36680	yweG	general stress protein	SigB									+
4.1	BSU_09690	ohrA		SigB									N/A
4.0	BSU_14660	ytxI		SigB									N/A
3.9	BSU_12150	ypjM		SigB									N/A
2.8	BSU_35830	yetG		SigB									N/A
2.8	BSU_04039	yocO		SigB									N/A
2.7	BSU_08490	yfkD		SigB						SigE	SigG		N/A
2.7	BSU_30900	ytkB		SigB									N/A
2.5	BSU_13020	yfkpA		SigB									N/A
2.3	BSU_16520	yvaB		SigB									N/A
2.3	BSU_28340	yocF		SigB									N/A
2.4	BSU_24750	ydhM		SigB							LexA		+
2.4	BSU_38180	yxeA		SigB									N/A
2.4	BSU_40450	yycO		SigB									N/A
2.4	BSU_07720	yfiD		SigB				AbrB					N/A
2.3	BSU_07700	yfiK		SigB				AbrB			Abh		N/A
2.2	BSU_39810	cstC		SigB									N/A
2.2	BSU_07550	yfiT		SigB									N/A
2.2	BSU_00170	yteV		SigB									N/A
2.2	BSU_38430	gspA		SigB									N/A
2.1	BSU_04220	ydbO		SigB									N/A
2.1	BSU_39840	yxkG		SigB									N/A
2.1	BSU_40529	yyaH	unknown	SigB									N/A
2.1	BSU_07900	ctaA	calcium export	SigB						SigG			N/A
2.0	BSU_03850	ydcQ	unknown	SigB									N/A
2.0	BSU_04450	ydiB		SigB						SigI			N/A
2.0	BSU_01360	yvaA	general stress protein	SigB						SigG			N/A
2.0	BSU_00160	yteU		SigB						SigA	SpoIIID		N/A
2.0	BSU_03410	yqzD		SigB				AbrB					N/A
2.0	BSU_06560	yerO		SigB									N/A
2.0	BSU_04160	ydeT		SigB									N/A
2.0	BSU_04710	rsbV	anti-anti-SigB	SigB	CcpA							SigA	N/A
2.0	BSU_02100	ispC	biosynthesis of beta-hydroxy fatty acid	SigB									N/A
2.0	BSU_38610	yusF	general stress protein	SigB						SigG			N/A
2.0	BSU_11839	ydiE		SigB									N/A
2.0	BSU_40070	ydiO	similar to permease	SigB									N/A
2.7	BSU_08510	yfkT		SigB						SigF	SigG		N/A
2.7	BSU_16310	yvaC	ea	SigB									N/A
2.7	BSU_02830	yuxF		SigB									N/A
2.7	BSU_02110	ykuB		SigB									N/A
2.7	BSU_07860	yfkJ		SigB								SigA	N/A
2.6	BSU_04720	rsbW	anti-sigma factor to SigB	SigB	CcpA							SigA	N/A
2.6	BSU_09240	yvcE	general stress protein	SigB									N/A
2.6	BSU_07930	yfkO		SigB						SigG			N/A
2.6	BSU_38830	ykrT		SigB									N/A
2.6	BSU_04380	ydaT		SigB									N/A
2.6	BSU_39720	yweD		SigB									N/A
2.6	BSU_04430	ydbD		SigB									N/A
2.5	BSU_39960	yxlB		SigB				AbrB				SigA	N/A
2.5	BSU_40030	yxaB		SigB									N/A
2.5	BSU_40060	yxrD		SigB									N/A
2.5	BSU_39050	katA		SigB							SigH		N/A
2.4	BSU_29760	yhcD		SigB									N/A
2.4	BSU_02360	yuzP		SigB						SigF	RsfA		N/A
2.4	BSU_38630	katG		SigB									N/A
2.4	BSU_05760	ydhK		SigB						SigE	SpoIIID		N/A
2.3	BSU_31260	yxjO		SigB									N/A
2.3	BSU_13169	ykzW		SigB						SigF	SigG		N/A
2.3	BSU_09140	yhcM		SigB									N/A
2.3	BSU_30640	ykrC	similar to eucalyptic amidase	SigB									N/A
2.2	BSU_07980	yfkl	general stress protein	SigB								SigA	N/A
2.1	BSU_00630	ctsR	regulation of protein degradation	SigB			Spx			SigF	SigM	CtsR	SigA	+
2.1	BSU_07900	yfkU		SigB									SigA	N/A
2.0	BSU_09770	ytzH	general stress protein	SigB							SigH		N/A
2.0	BSU_27700	bofC		SigB	CcpA					SigF	SigG		N/A
2.0	BSU_19150	ycnB		SigB									N/A
2.0	BSU_13940	spo0E	Spo0A-P phosphatase	SigB				AbrB			Rok	SigA	N/A
2.0	BSU_31270	yuxK	unknown	SigB						SigE	SpoIIID		N/A
1.9	BSU_09450	yhdF	similar to glucose 1-dehydrogenase	SigB							CtsR	SigA	N/A
1.9	BSU_00840	mcsA	control of ClpE activity	SigB			Spx			SigF	SigM	CtsR	SigA	+
1.9	BSU_29760	yhcJ		SigB							SigH		N/A
1.9	BSU_35180	ydaR	general stress protein	SigB								SigA	N/A
1.9	BSU_00320	ytn		SigB								SigA	N/A
1.8	BSU_03200	yotE		SigB									N/A
1.8	BSU_00850	mcsB	control of ClpE activity	SigB			Spx			SigF	SigM	CtsR	SigA	+
1.6	BSU_38720	yteO	general stress protein	SigB									N/A
1.6	BSU_27740	cstO		SigB	CcpA					SigF	SigG		N/A
1.6	BSU_07720	yfiE		SigB				AbrB					N/A
1.6	BSU_06400	yocC	unknown	SigB									N/A
10.1	BSU_18950	ymfL	unknown	LexA									N/A
4.2	BSU_06220	yfjO	unknown										N/A
4.2	BSU_03222	recA	co-sigma factor SigO	YvrHb						SigO	RecA		+
4.0	BSU_21150	yvnB	unknown										N/A
3.3	BSU_24670	comGB	genetic competence, DNA uptake	ComK						SigF		SigA	N/A
3.0	BSU_07570	yfiS	malate transporter	MalR									N/A
2.9	BSU_12270	ydjB	unknown										N/A
2.7	BSU_39440	yvcE	unknown										N/A
2.6	BSU_38870	yteA	unknown										N/A
2.5	BSU_22960	yolA	unknown							SigF			N/A
2.5	BSU_36970	spo0B	control of Sig0 activation							SigF			N/A
2.4	BSU_07340	pel	degradation of polygalacturonic acid	ComA	TnrA	CcpA							N/A
2.2	BSU_13650	mtg	small membrane protein										N/A
2.2	BSU_07250	yxlD	NADPH-cytochrome P450 reductase										N/A
2.1	BSU_00660	yteT	DNA integrity during spore development							SigF			+
2.1	BSU_22900	ytpF	unknown										N/A
2.1	BSU_26970	ecfM	forespore-specific protein							SigG			N/A
2.0	BSU_03620	bcrA	regulation of resistance to salicylic acid										N/A
2.0	BSU_07630	yfiF	unknown										N/A
2.0	BSU_18360	sweA	inhibits cell separation	WalR									N/A
1.9	BSU_26480	yqhG	sporulation										N/A
1.9	BSU_31322	ypqP	potassium exporter	SinR									N/A
1.8	BSU_14150	ctaM	cell-cAMP binding protein	SpoIIA		CcpA							N/A
1.8	BSU_36510	ngg	antimicrobial uptake		TnrA							SigA	+
1.8	BSU_37870	spsM	spore coat polysaccharide synthesis	GerE						SigE	SigK		N/A
1.7	BSU_39070	acuB	acetoin utilization	AcoR		CcpA					SigL		N/A
1.7	BSU_13760	yfkY	sporulation								SigK		N/A
1.7	BSU_12020	manR	mannose uptake and utilization	ManR								SigA	N/A
1.6	BSU_12010	manP		ManR								SigA	N/A
1.7	BSU_34920	hisD	biosynthesis of histidine										+
1.7	BSU_34900	hisE											N/A
1.6	BSU_34900	hisZ	histidyl-tRNA synthetase										N/A
1.7	BSU_13520	ykvF	unknown										N/A
1.7	BSU_21830	ezfG	NADH dehydrogenase										N/A
1.7	BSU_02200	ykfB	putative peptidoglycan binding protein										+
1.6	BSU_39470	acoD	thiamethylmalate decarboxylase	CymR								SigA	N/A
1.6	BSU_39460	yvnD	uptake and utilization of S-(2-succino)cysteine	CymR								SigA		
1.6	BSU_36320	ykfM	unknown	YvbU									+
1.6	BSU_03660	yclG	unknown							SigF			N/A
1.6	BSU_22950	ywcE	involved in spore envelope assembly							SigF			N/A
1.6	BSU_33590	yvaG	similar to Jvszvsgd- zuyvdetter-protein reductase										N/A
1.5	BSU_27040	bioD	thiolase uptake and phosphorylation	LevR		CcpA					SigL		+
1.5	BSU_37040	yxkM	unknown	MalR								SigA	N/A
1.5	BSU_04470	dctP	uptake of succinate, fumarate, malate and oxaloacetate			CcpA						SigA	N/A
7.0	BSU_12672	xkdA	PBSX										+
2.5	BSU_12560	xkrA											
2.5	BSU_12605	xkdV											
4.7	BSU_12561	xpt											
4.1	BSU_12600	xtrB											
4.0	BSU_12601	xkdT											
4.0	BSU_12763	xkdW											
3.9	BSU_12610	xkdG											
3.9	BSU_12640	xkdJ											
3.9	BSU_12571	xkdN											
3.9	BSU_12540	xkdO											
3.8	BSU_12580	xkdP											
3.8	BSU_12619	ykzL											
3.8	BSU_12570	xtmA											
3.7	BSU_12720	xkdQ											
3.6	BSU_12760	xepA											
3.5	BSU_12530	xkdC											
3.4	BSU_12749	xkdA											
3.3	BSU_12460	xdjB											
3.3	BSU_12600	xkdM											
3.3	BSU_12960	xkdM											
3.3	BSU_12740	xkdU											
3.3	BSU_12590	xkdE											
2.9	BSU_12700	xkdQ											
2.7	BSU_12580	xmlB											
2.7	BSU_12760	xtaA											
2.7	BSU_12730	xkdT											
2.5	BSU_12649	ykzM											
2.5	BSU_12810	xtpA											
2.5	BSU_12750	xkdV											
2.5	BSU_12630	xkdI											
2.4	BSU_12661	xkdQ											
9.5	BSU_21229	yvcA	SPβ										+
4.2	BSU_21160	yorA											
3.6	BSU_21070	yorJ											
3.6	BSU_21220	yomU											
3.6	BSU_21100	yorG											
3.2	BSU_21130	yorD											
3.2	BSU_21110	yorF											
3.1	BSU_21210	yomV											
3.1	BSU_21140	yorC											
3.0	BSU_21200	yomW											
2.9	BSU_21090	yorH											
2.8	BSU_20450	yocA											
2.7	BSU_21160	yomK											
2.7	BSU_21300	yomM											
2.6	BSU_21250	yomR											
2.2	BSU_21360	yomE											
1.7	BSU_20060	ydbB											

Table S2. RNA-seq analysis of genes downregulated in (CH* + 10.0 mM $MgCl_2$)/(CH*).

Fold-change	Gene ID	Gene	Description	Regulon	Deletion strain Mg^{2+} responsive?
0.4	BSU_39230	*wapA*	intercellular competition	YvrHb WalR DegU SigA	+
0.5	BSU_39220	*wapI*		YvrHb WalR DegU SigA	N/A
0.5	BSU_10770	*wprA*	secreted quality control protease	YvrHb CcpA SigA	+
0.6	BSU_21440	*bdbB*	thiol-disulfide oxidoreductase	YvrHb AbrB Abh DnaA Rok	N/A
0.6	BSU_23090	*rsiX*	control of SigX activity	YvrHb SigX SigA	N/A
0.6	BSU_23100	*sigX*	resistance to cationic antimcrobial peptides	YvrHb SigX SigA	+
0.6	BSU_38520	*dltC*	biosynthesis of teichoic acid	YvrHb Spo0A SigD SigM SigX SigV	+
0.7	BSU_38540	*dltE*		YvrHb Spo0A SigD SigM SigX SigV	N/A
0.7	BSU_38510	*dltB*		YvrHb Spo0A SigD SigM SigX SigV	N/A
0.7	BSU_38530	*dltD*		YvrHb Spo0A SigD SigM SigX SigV	+
0.5	BSU_27180	*yrhH*	similar to methyltransferase	SigM SigX SigW	+
0.6	BSU_05470	*mneP*	primary manganese (II) efflux pump	MntR SigA	N/A
0.6	BSU_34430	*racX*	production of non-canonical D-amino acids	SigW	+
0.6	BSU_16950	*pbpX*	penicillin-binding protein X	SigM SigX SigV	N/A
0.6	BSU_23830	*yqjL*	general stress protein,	SigB SigM SigW SigV	+
0.6	BSU_17840	*fosB*	bacillithiol-S-transferase	SigW	+
0.7	BSU_14480	*abh*	transcriptional regulator of transition state genes	SigM SigX SigV	+
0.7	BSU_08760	*spo0M*	sporulation-control gene	SigH SigW	N/A
0.7	BSU_30000	*ythQ*	similar to ABC transporter	SigW	N/A
0.2	BSU_33490	*cadA*	cadmium transporting ATPase	CzrA SigA	+
0.5	BSU_04120	*yczI*	unknown		+
0.5	BSU_26650	*czcD*	cation efflux	CzrA	+
0.5	BSU_27809	*yrzT*	unknown		N/A
0.6	BSU_39120	*yxiM*	similar to rhamnogalacturonan acetylesterase		N/A
0.5	BSU_39140	*yxiK*	unknown		N/A
0.5	BSU_39150	*yxiJ*			+
0.6	BSU_39160	*yxiI*			N/A
0.5	BSU_39170	*yxzG*			+
0.6	BSU_39180	*yxiH*			+
0.7	BSU_39190	*yxiG*			+
0.4	BSU_39200	*yxzC*			+
0.5	BSU_39210	*yxiF*			N/A
0.6	BSU_04540	*ydbO*	similar to cation efflux system		N/A
0.6	BSU_20560	*yoqO*	unknown		N/A
0.6	BSU_21530	*yolB*	similar to phage-related protein	AbrB	N/A
0.6	BSU_21540	*yolA*	unknown	AbrB	N/A
0.6	BSU_23328	*ypzJ*	unknown		+
0.6	BSU_26640	*trkA*	cation export	CzrA	+
0.7	BSU_09660	*yheN*	putative polysaccharide deacetylase		N/A

Table S3. Deletion strains that retained the Mg^{2+}-dependent cell shortening phenotype

strain*	genotype	BKK strain	function	Description	Deletion strain Mg^{2+} responsive?
BJH582	Δ*dctS*	BKK04450	kinase	regulation of the dctS-dctR-dctP operon	+
BJH583	Δ*glnK*	BKK02440	kinase	regulation of the glsA-glnT operon	+
BJH585	Δ*ydfI*	BKK05420	regulator	control of ydfJ expression	+
BJH586	Δ*kinC*	BKK14490	kinase	initiation of sporulation	+
BJH587	Δ*cheA*	BKK16430	kinase	modulation of flagellar switch bias	+
BJH588	Δ*lytT*	BKK28920	regulator	control of pyruvate utilization	+
BJH589	Δ*desK*	BKK19190	kinase	regulation of cold shock expression of des	+
BJH590	Δ*ybdK*	BKK02010	kinase	unknown	+
BJH591	Δ*ykoH*	BKK13260	kinase	unknown	+
BJH592	Δ*yhcY*	BKK09320	kinase	unknown	+
BJH593	Δ*bceS*	BKK30390	kinase	resistance against toxic peptides	+
BJH594	Δ*citS*	BKK07580	kinase	regulation of citrate uptake	+
BJH595	Δ*yxjL*	BKK38910	regulator	unknown	+
BJH596	Δ*yesM*	BKK06950	kinase	unknown	+
BJH597	Δ*yrkQ*	BKK26420	kinase	unknown	+
BJH598	Δ*liaS*	BKK33090	kinase	regulation of the liaI-liaH-liaG-liaF-liaS-liaR operon	+
BJH599	Δ*lnrJ*	BKK08290	kinase	resistance to linearmycin	+
BJH600	Δ*natK*	BKK02730	kinase	regulation of the natA-natB operon	+
BJH601	Δ*yclK*	BKK03760	kinase	unknown	+
BJH602	Δ*resE*	BKK23110	kinase	regulation of aerobic and anaerobic respiration	+
BJH605	Δ*yxjM*	BKK38900	kinase	unknown	+
BJH609	Δ*comP*	BKK31690	kinase	regulation of genetic competence and quorum sensing	+
BJH610	Δ*spo0A*	BKK24220	regulator	initiation of sporulation	+
BJH611	Δ*cssS*	BKK33020	kinase	control of cellular responses to protein secretion stress	+
BJH612	Δ*degS*	BKK35500	kinase	regulation of degradative enzymes, genetic competence, and other adaptive responses	+
BJH613	Δ*yvrG*	BKK33210	kinase	regulation cell surface maintenance	+
BJH615	Δ*resD*	BKK23120	regulator	regulation of aerobic and anaerobic respiration	+
BJH616	Δ*ypsdS*	BKK34710	kinase	resistance against toxic peptides	+
BJH617	Δ*yvfT*	BKK34070	kinase	unknown	+
BJH618	Δ*psdR*	BKK34720	regulator	resistance against toxic peptides	+
BJH621	Δ*glnL*	BKK02450	regulator	regulation of the glsA-glnT operon	+
BJH622	Δ*cheY*	BKK16330	regulator	modulation of flagellar switch bias	+
BJH623	Δ*yneI*	BKK17940	regulator	unknown	+
BJH624	Δ*lytS*	BKK28930	kinase	control of pyruvate utilization	+
BJH626	Δ*ydfH*	BKK05410	kinase	control of ydfJ expression	+
BJH638	Δ*malK*	BKK31520	kinase	regulation of malate uptake	+
BAS206	Δ6			*Bacillus subtilis* 168 ΔSPβ Δskin ΔPBSX Δprophage 1 pks::cat Δprophage 3	+

*All BKK-based strains were generated by introducting genomic DNA from the indicated BKK strain into *B. subtilis 168* competent cells and selecting for kanamycin resistance.

Table S4. Strains

Strain	Wildtype (WT) Strains	Reference
BJH004	*Bacillus subtilis* 168 *trpC2*	Bacillus Genetic Stock Center 1A1
BJH001	PY79	Obtained from David Rudner (1)
BJH403	3610	Dan Kearns (2)
BTG169	*Bacillus subtilis* 168 *trpC+*	This study
BAS206	Δ*6* (Δ*SPβ* Δ*skin* Δ*PBSX* Δ*prophage 1 pks::cat* Δ*prophage 3*)	Obtained from Ryland Young who acquired from Dean Scholl (3, 4)
	***Bacillus subtilis* 168 derivatives**	
BTG182	*amyE::P_{mgtE} leader (nt -486 - +25)-lacZ (cat)*	Wade Winkler (5)
BTG333	*mpfA::kan, amyE::P_{mgtE} leader (nt -486 - +25)-lacZ (cat)*	This study
BTG186	*amyE::P_{xyl}-gfp-zapA (cat)*	This study
BTG185	*amyE::P_{spac}-ftsZ-gfp (cat)*	This study
BTG708	*amyE::P_{hy}-uppS (spec)*	This study
BTG697	*amyE::P_{hy}-RBS- mraY (spec)*	This study
BTG678	*amyE::Phy-RBS-bcrC (spec)*	This study

Table S5. Plasmids

Plasmid	Description	Reference
pDR111	*amyE::P_{hy} (spec)(amp)*	David Rudner

Table S6. Oligonucleotides

OLIGO	SEQUENCE 5' TO 3'
OTG109	AATCCCAATCGCCCCAAAGGCTCCGGAGGCAG
OTG110	CATAGTAGTTCCTCCTTATGTAAGCTTAATTG
OTG215	GCTAGCCGCATGCAAGCTAAT
OTG216	CTGCTTCATTTTCTCATCTCTTCAG
OTG275	GGATAACAATTAAGCTTACATAAGGAGGAACTACTATGAACTACGAAATTTTTAAAGCAATCCATG
OTG276	TTCCACCGAATTAGCTTGCATGCGGCTAGC CTTTCTTAGAAATTTTGATCGGTTGG
OTG287	GGATAACAATTAAGCTTACATAAGGAGGAACTACTATGCTTGAGCAAGTCATTCTGTTT
OTG288	TTCCACCGAATTAGCTTGCATGCGGCTAGC CATTTTCCACTTATAACCACACCT
OTG309	GGATAACAATTAAGCTTACATAAGGAGGAACTACTATGCTCAACATACTCAAAAATTGG
OTG310	TTCCACCGAATTAGCTTGCATGCGGCTAGCCCACCATCCTCTAAATTCCGCCAA

Text S1. Strain construction

Strain construction (in alpha-numerical order)

The *B. subtilis* kanamycin resistant deletion strains in Table S3 were derived from the BKK collection (6). Genomic DNA from each BKK strain was transformed into competent BJH004 and selection was performed on LB containing 10 µg ml-1 kanamycin.

BTG169 *B. subtilis 168 trpC2*+ was generated by transforming BJH004 with 40 ng of genomic DNA from PY79 and selecting for growth on minimal medium lacking tryptophan. The strain was confirmed to harbor the PY79 *trpC* allele using whole genome sequencing.

BTG182 [*amyE::P_{mgtE} leader (nt -486 - +25)-lacZ (cat)*] was created by transforming *Bs168* with genomic DNA from bCAW2036 [*amyE::P_{mgtE} leader (nt -486 - +25)-lacZ (cat)*] selecting for growth on LB plates containing 7.5 µg ml-1 chloramphenicol.

BTG185 [*amyE::P_{spac}-ftsZ-gfp (cat)*] was created by transforming *Bs168* with genomic DNA from gJW28 [*amyE::P_{spac}-ftsZ-gfp (cat)*] selecting for growth on LB plates containing 7.5 µg ml-1 chloramphenicol.

BTG186 [*amyE::P_{xyl}-gfp-zapA (cat)*] was created by transforming *Bs168* with genomic DNA from gJW29 [*amyE::P_{xyl}-gfp-zapA (cat)*] selecting for growth on LB plates containing 7.5 µg ml-1 chloramphenicol.

BTG333 [*mpfA::kan, amyE::P_{mgtE} leader (nt -486 - +25)-lacZ (cat)*] was created by transforming BJH681 [*mpfA::kan*] with genomic DNA from bCAW2036 [*amyE::P_{mgtE} leader (nt -486 - +25)-lacZ (cat)*] selecting for growth on LB plates containing 7.5 µg ml-1 chloramphenicol.

BTG678 [*amyE::P_{hy}-bcrC (spec)*] was created by transforming *Bs168* with a linear Gibson assembly product encoding three fragments including a region upstream of *amyE* with a spectinomycin cassette using oTG109 and oTG110, the *$P_{hyperspank}$-bcrC* using oTG275 and oTG276, a region downstream of *amyE* into *B. subtilis* 168 using oTG215 and oTG216 and selecting for for growth on LB plates containing 100 µg ml-1 spectinomycin. The detailed protocol is available in reference (7).

BTG697 [*amyE::P_{hy}-RBS- mraY (spec)*] was created by transforming *Bs168* with a linear Gibson assembly product encoding three fragments including a region upstream of *amyE* with a spectinomycin cassette using oTG109 and oTG110, the *$P_{hyperspank}$-mraY* using oTG287 and oTG288, a region downstream of *amyE* into *B. subtilis* 168 using

oTG215 and oTG216 and selecting for for growth on LB plates containing 100 µg ml-1 spectinomycin. The detailed protocol is available in reference (7).

BTG708 [*amyE::*P_{hy}*-uppS (spec)*] was created by transforming *Bs168* with a linear Gibson assembly product encoding three fragments including a region upstream of *amyE* with a spectinomycin cassette using oTG109 and oTG110, the $P_{hyperspank}$*-uppS* using oJH309 and oJH310, a region downstream of *amyE* into *B. subtilis* 168 using oTG215 and oTG216 and selecting for for growth on LB plates containing 100 µg ml-1 spectinomycin. The detailed protocol is available in reference (7).

REFERENCES

1. Youngman P, Perkins JB, Losick R. 1984. Construction of a cloning site near one end of Tn917 into which foreign DNA may be inserted without affecting transposition in *Bacillus subtilis* or expression of the transposon-borne erm gene. Plasmid 12:1-9.
2. Konkol MA, Blair KM, Kearns DB. 2013. Plasmid-encoded ComI inhibits competence in the ancestral 3610 strain of *Bacillus subtilis*. J Bacteriol 195:4085-93.
3. Reuss DR, Thurmer A, Daniel R, Quax WJ, Stulke J. 2016. Complete genome sequence of *Bacillus subtilis subsp. subtilis* Strain 6. Genome Announc 4.
4. Westers H, Dorenbos R, van Dijl JM, Kabel J, Flanagan T, Devine KM, Jude F, Seror SJ, Beekman AC, Darmon E, Eschevins C, de Jong A, Bron S, Kuipers OP, Albertini AM, Antelmann H, Hecker M, Zamboni N, Sauer U, Bruand C, Ehrlich DS, Alonso JC, Salas M, Quax WJ. 2003. Genome engineering reveals large dispensable regions in *Bacillus subtilis*. Mol Biol Evol 20:2076-90.
5. Dann CE, 3rd, Wakeman CA, Sieling CL, Baker SC, Irnov I, Winkler WC. 2007. Structure and mechanism of a metal-sensing regulatory RNA. Cell 130:878-92.
6. Koo BM, Kritikos G, Farelli JD, Todor H, Tong K, Kimsey H, Wapinski I, Galardini M, Cabal A, Peters JM, Hachmann AB, Rudner DZ, Allen KN, Typas A, Gross CA. 2017. Construction and analysis of two genome-scale deletion libraries for *Bacillus subtilis*. Cell Syst 4:291-305 e7.
7. Duan Y, Sperber AM, Herman JK. 2016. YodL and YisK possess shape-modifying activities that are suppressed by mutations in *Bacillus subtilis mreB* and *mbl*. J Bacteriol 198:2074-88.